HIGH-RESOLUTION LASER EXCITATION SPECTROSCOPY OF METAL-CONTAINING FREE RADICALS USING A SUPERSONIC MOLECULAR BEAM SPECTROMETER

by

Chunfeng Zhao

A thesis
Presented to the University of Waterloo
in fulfilment of the
thesis requirement for the degree of
Doctor of Philosophy
in
Chemistry

Waterloo, Ontario, Canada, 1997

The University of Waterloo requires the signatures of all persons using or photocopying this thesis. Please sign below, and give address and date.

ABSTRACT

This thesis describes the building of a new supersonic molecular beam, laser-induced fluorescence spectrometer and its application to the spectroscopy of various metal containing radicals. Using this spectrometer, laser vaporized metals (Ca and Sr) react with reactants such as D_2O, NH_3 and $HOCH_3$ and, because of the cooling effect of the supersonic molecular beam, rotationally resolved spectra can be obtained for some larger molecules.

The SrOD $\tilde{B}^2\Sigma^+ - \tilde{X}^2\Sigma^+$ spectrum was recorded and analyzed and improved molecular parameters were derived. The high resolution $\tilde{B}^2B_1 - \tilde{X}^2A_1$ and the $\tilde{C}^2A_1 - \tilde{X}^2A_1$ spectra of $CaNH_2$ were studied, to give the molecular constants for the $\tilde{B}^2B_1$ and $\tilde{C}^2A_1$ states. The high resolution $\tilde{C}^2A_1 - \tilde{X}^2A_1$ transition of $SrNH_2$ was analyzed to derive the molecular constants for the $\tilde{C}^2A_1$ state. Finally, The $\tilde{A}^2E - \tilde{X}^2A_1$ transition of $CaOCH_3$ was analyzed and discussed.

ACKNOWLEDGEMENTS

I would like to thank Peter Bernath and John Hepburn for their advice and support throughout my graduate study at Waterloo.

I also thanks for the group members who gave me their honest help.

To my Mother, Father and Wenjun

TABLE OF CONTENTS

LIST OF TABLES

LIST OF ILLUSTRATIONS

CHAPTER 1

INTRODUCTION

1.1 Introduction

The interaction of metals with organic molecules is very important in modern chemistry, because of the possibility of applications and the variety of molecules can be synthesized. Synthetic chemists usually use NMR and X-ray crystallography to characterize the products of reactions. These reactions occur in solution or in the solid state and are often influenced by the presence of a solvent. In recent years, laser spectroscopy has been introduced to study metal-ligand chemistry in the gas phase, which makes it possible to study reactions without the effect of solvents.

During the past ten years the reactions of gas phase alkaline metals with inorganic and organic molecules have been studied intensively by means of laser excitation spectroscopy. The use of laser evaporation coupled with supersonic expansion makes it easier to record rotationally cooled spectra of a variety of molecules. These powerful methods have revolutionized the way chemists analyze reactions, and made it possible to determine the molecular geometry of many diatomic, triatomic and larger molecules with high accuracy.

The study of metal-containing free radicals in the gas phase has been a hot topic since the 1980s. Free radicals are atoms or molecular fragments containing one or more unpaired electrons. Because they are highly reactive and short-lived, they have to be

synthesized and analyzed *in situ.* Many free radicals are formed in high temperature systems such as in flames (1) or in the atmospheres of stars (2). The invention of the metal flow reactor, the Broida oven, made it possible to prepare and analyze many different kinds of metal-containing free radicals.

The gas-phase alkaline earth metal halides, like CaF and SrF, were the first members of the alkaline earth family of radicals to be synthesized and characterized (3-8). Then the isoelectronic alkaline earth metal monohydroxides (MOH, M = Ca, Sr, Ba) were discovered (9) and they were the subject of several spectroscopic investigations (10-15). It was the laser excitation technique that made it possible to study gaseous inorganic molecules containing larger ligands such as amide (16, 17), alkoxide (18-20), azide (20), methyl (22), isocyanate (23, 24) and cyclopentadienide (25).

CaOH and SrOH are very reactive and can only be isolated for extended periods of time in rare gas matrices. However, substantial concentrations are found in a variety of energetic environments such as in flames (1) and exploding fireworks (26, 27). They are also thought to be abundant in the atmospheres of cool stars (28) and in the earth's upper atmosphere (29,30). It was found that the alkaline earth hydroxides were easily made in a Broida oven (16, 31, 32). The combination of a relatively cool molecular source (~500 K, much less than the traditional arcs or carbon furnaces) and single frequency tunable dye laser excitation that made detailed analysis of the spectra possible for some simple molecules. In this way a new family of isoelectronic derivatives, the alkaline earth

monoamides, $CaNH_2$, $SrNH_2$ and $BaNH_2$ were discovered (16, 34). Some of the transitions were also studied in a supersonic jet, and the spectra were rotationally analyzed (35, 36).

Another important discovery was the laser-driven chemical reaction of alkaline earth metals (23, 24). Ground state Ca and Sr vapors react with only a few molecules. For most of the molecules studied, it was found that laser excitation of the metal atom promotes the chemical reactivity of Ca, Sr and Ba vapors. In this case, one laser is used to drive the chemical reaction while a second laser detects the product. This laser driven chemical reactivity was vital in the preparation of most of the free radicals studied in a Broida oven.

The species made in a Broida oven are called high temperature molecules because the metal is vaporized at high temperature. It is possible to rotationally analyze the spectra of some simple molecules like CaOH using a Broida oven but for large molecules such as $CaOCCH_3$ lower temperatures are required in order to resolve the rotational structure. In this case a laser-vaporization source coupled with a supersonic expansion into vacuum and laser detection is very convenient.

The subject of this dissertation is the construction of a supersonic molecular beam spectrometer and the study of gas phase metal-containing free radicals using high resolution laser excitation spectroscopy. A laser evaporation apparatus was built to perform the spectroscopic studies. Metals (Ca and Sr) are vaporized by a pulsed

Nd/YAG laser, and then reacted with D_2O, NH_3 or $HOCH_3$ present in an inert gas (Ar, Ne or He). A cw dye ring laser was used to excite laser-induced fluorescence. All the molecules discussed in this thesis consist of a single metal atom (Ca or Sr), bonded to a single ligand (OD, NH_2 or OCH_3).

SrOD (chapter 3) was the first molecule studied in our molecular beam spectrometer because it is easy to make and the bands were identified (16) previously. The alignment of the system was not optimized at that time, and the spectrum could only be recorded when He was used as a carrier gas. Attempts to record the spectrum with Ar failed. The spectrum was analyzed and improved molecular parameters were derived.

In chapter 4 the high resolution $\tilde{B}^2B_1 - \tilde{X}^2A_1$ and the $\tilde{C}^2A_1 - \tilde{X}^2A_1$ transitions of $CaNH_2$ will be discussed. By then the spectrometer was optimized and very good spectra were obtained even in Ar.

The high resolution $\tilde{C}^2A_1 - \tilde{X}^2A_1$ transition of $SrNH_2$ was studied and the results are reported in chapter 5. The spectrum was recorded both in Ar and He. Because the spectrum was very dense the analysis was not easy. A good set of molecular constants were derived.

Chapter 6 describes the work on the symmetric top calcium monomethoxide, $CaOCH_3$. The $\tilde{A}^2E - \tilde{X}^2A_1$ transition was analyzed and the results are discussed.

1.2 References

1. C. Th. J. Alkemade, Tj. Hollander, W. Snelleman and P. J. Th. Zeegers, "Metal Vapors in Flames", Pergamon Press, Oxford, 1982.

2. T. Tsuji, Astron. Astrophys. 23, 411 (1973).

3. L. de Boisbaudran, Compt. Rend. 69, 455 (1869).

4. R. C. Johnson, Proc. Roy. Soc. London 133, 336 (1931).

5. R.W. Field, D.O. Harris and T. Tanaka, J. Mol. Spectrosc. 57, 107 (1975).

6. J. Nakagawa, P.J. Domaille, T.C. Steimle and D.O. Harris, J. Mol. Spectrosc. 70, 347 (1978).

7. P.F. Bernath and R.W. Field, J. Mol. Spectrosc. 82, 339 (1980).

8. M. Dulick, P.F. Bernath and R.W. Field, Can. J. Phys. 58, 703 (1980).

9. J.F.W. Herschel, Trans. Roy. Soc. Edinburgh 9, 445 (1823).

10. J. Nakagawa, R.F. Wormsbecher and D.O. Harris, J. Mol. Spectrosc. 97, 37 (1983).

11. R.C. Hilborn, Q. Zhu and D.O. Harris, J. Mol. Spectrosc. 97, 73 (1983).

12. P.F. Bernath and S. Kinsey-Nielsen, Chem. Phys. Lett. 105, 663 (1984).

13. C. R. Brazier and P.F. Bernath, J. Mol. Spectrosc. 114, 163 (1985).

14. P.F. Bernath and C.R. Brazier, Astrophys. J. 288, 373 (1985).

15. S. Kinsey-Nielsen, C. R. Brazier and P.F. Bernath, J. Chem. Phys. 84, 698 (1986).

16. R.F. Wormsbecher, M. Trukula, C. Martner, R.E. Penn and D.O. Harris,

J. Mol. Spectrosc. 97, 29 (1983).

17. R.F. Wormsbecher, R.E. Penn and D.O. Harris, J. Mol. Spectrosc. 97, 65 (1983).

18. C. R. Brazier , P.F. Bernath, S. Kinsey-Nielsen and L.C. Ellingboe,

J. Chem. Phys. 82, 1043 (1985).

19. C. R. Brazier and L.C. Ellingboe, S. Kinsey-Nielsen, and P.F. Bernath,

J. Am. Chem. Soc. 108, 2126 (1986).

20. L.C. O'Brien, C. R. Brazier and P.F. Bernath, J. Mol. Spectrosc. 130. 33 (1988)

21. C. R. Brazier and P.F. Bernath, J. Chem. Phys. 88, 2112 (1988).

22. C. R. Brazier and P.F. Bernath, J. Chem. Phys. 86, 5918 (1987).

23. L.C. Ellingboe, A.M.R.P. Bopegedera, C.R. Brazier and P.F. Bernath.

Chem. Phys. Lett. 126, 285 (1986).

24. L.C. O'Brien and P.F. Bernath, J. Chem. Phys. 88, 2117 (1988).

25. L.C. O'Brien and P.F. Bernath, J. Am. Chem. Soc. 108, 5017 (1986).

26. C.G. James and T.M. Sugden, Nature 175, 333 (1955).

27. M. Charton and A.G. Gaydon, Proc. Phys. Soc. London A. 69, 520 (1956);

A.G. Gaydon, Proc. Roy. Soc. London A. 231, 437 (1955).

28. T. Tsuji, Astron. Astrophys. 23, 411 (1973).

29. S. Drapatz, L. Haser and K.W. Michel, Z. Naturforsch. 29A, 411 (1974).

30. E. Murad, W. Swider and S.W. Benson, Nature 289, 273 (1981).

31. J. Nakagawa, R.F. Wormsbecher and D.O. Harris, J. Mol. Spectrosc., 97, 37(1983).

32. R.C. Hilborn, Q. Zhu, D.O. Suenram, J. Mol. Spectrosc. 97, 73(1983).

33. R.F. Wormsbecher, R.E. Penn and D.O. Harris, J. Mol. Spectrosc. 97, 65 (1983).

35. C.J. Whithman and Ch. Jungen, J. Chem. Phys. 93, 15 (1990).

36. A.J. Marr, M. Tanimoto, D. Goodridge, and T.C. Steimle,

J. Chem. Phys. 103, 15 (1995).

CHAPTER 2

EXPERIMENTAL

The experimental setup is a combination of a laser ablation source and a supersonic molecular beam expansion system. The metal vapors of strontium or calcium are produced by laser ablation, then mixed with the reactants and expanded into vacuum through a supersonic expansion. The spectrum is recorded by detecting the laser induced fluorescence. The details of the supersonic molecular beam spectrometer will be discussed in the following sections.

The block diagram of the experimental apparatus is given in Figure (2.1). The apparatus has two separately pumped chambers. The ablation source chamber was pumped by a 10 in. diffusion pump (Edwards 250/200), while the detection chamber was pumped by a 4 in. diffusion pump (Edwards 100/300).

The molecular beam was produced by a pulsed valve. The second harmonic (532 nm) of a 10 Hz pulsed Nd:YAG laser was used to vaporize the metal. The beam was formed by expansion of 40 ~ 60 psi of helium or argon seeded with reactants. The stainless-steel nozzles can accept a metal sample rod with a diameter up to 8 mm. The rod was rotated and translated during the experiment. The ablation laser was weakly focused onto the sample and entered the sample holder through a 1-mm hole. The expansion channel was about 1 mm in diameter and 5 ~ 10 mm long.

The signal was detected by monitoring the laser-induced fluorescence (LIF) produced by the molecular beam when it intersected the probe laser beam from a cw-ring dye laser 15 cm downstream from the nozzle. A Hamamatsu photomultiplier tube (R943-02) was aligned perpendicular to both the molecular beam and the probe laser beam, and the LIF was collected through a lens assembly. A narrow bandpass filter (40 nm or 10 nm) centered at the laser frequency was used to reduce the effect of plasma emission and other non-resonant light. A boxcar integrator was used to process the LIF signal. A time "window" of 20 msec width was opened after a 80 μsec delay for He and 180 μsec delay for Ar from when the ablation laser fired. To increase the signal-to-noise ratio, a very slow laser scan (40 - 100 s /10 GHz) was used.

The Coherent Autoscan 699-29 dye ring laser was calibrated with the I_2 lines recorded at the same time during the experiment. The absolute accuracy of the line positions is about 0.003 cm^{-1}. Each part of the apparatus is described in detail in the following sections. Some of the necessary background information is also included.

2.1 Laser vaporization and the creation of small molecules

The conventional way of vaporizing metals is by heating them, for example in a Broida oven. For some low boiling point metals, it is convenient to produce metal vapor this way, however, for some refractory metals, such as tungsten, a specially designed and

expensive high temperature furnace is required. Because of the extremely high power density of laser light, it is possible to evaporate virtually any material. Ruby lasers (λ = 694 nm) (1), CO_2 TEA lasers(λ = 10 μm) (2), excimer lasers (λ = 308, 351 nm)(3) and Nd:YAG lasers (λ =266, 355, 532, 1069 nm) (4) have all been used to vaporize a variety of materials. In our experiment we used a Nd:YAG laser (λ = 532 nm) as the ablation source.

The laser power density at the surface of the solid material determines the physical processes that take place (5). Below about 10^5 W/cm^2 the surface is only heated. This results in thermal ejection of volatile species from the surface or from the bulk material. Between 10^5 and 10^8 W/cm^2, both melting and evaporation occur while at power densities that exceed 10^9 W/cm^2 the vaporization (atomization) of the material is dominant. At this high power density level the electrical properties and melting points of the material play virtually no role in the vaporization process because of the extreme physical conditions. A very dense vapor cloud results from laser ablation. Stimulated Raman scattering of the incident radiation creates many high order anti-Stokes photons that lead to multiphoton ionization or even direct single photon ionization of the material. The plasma is formed when the laser power density exceeds the plasma ignition thresholds (6,7). Normally up to 90 % of the incident radiation is absorbed by the plasma (8). The number of atoms that is vaporized by a single pulse from a Q-switched laser is reported to range between 10^{13} to 10^{17} atoms per laser shot (9 -12), the exact number being determined by the power density in combination with the irradiated area.

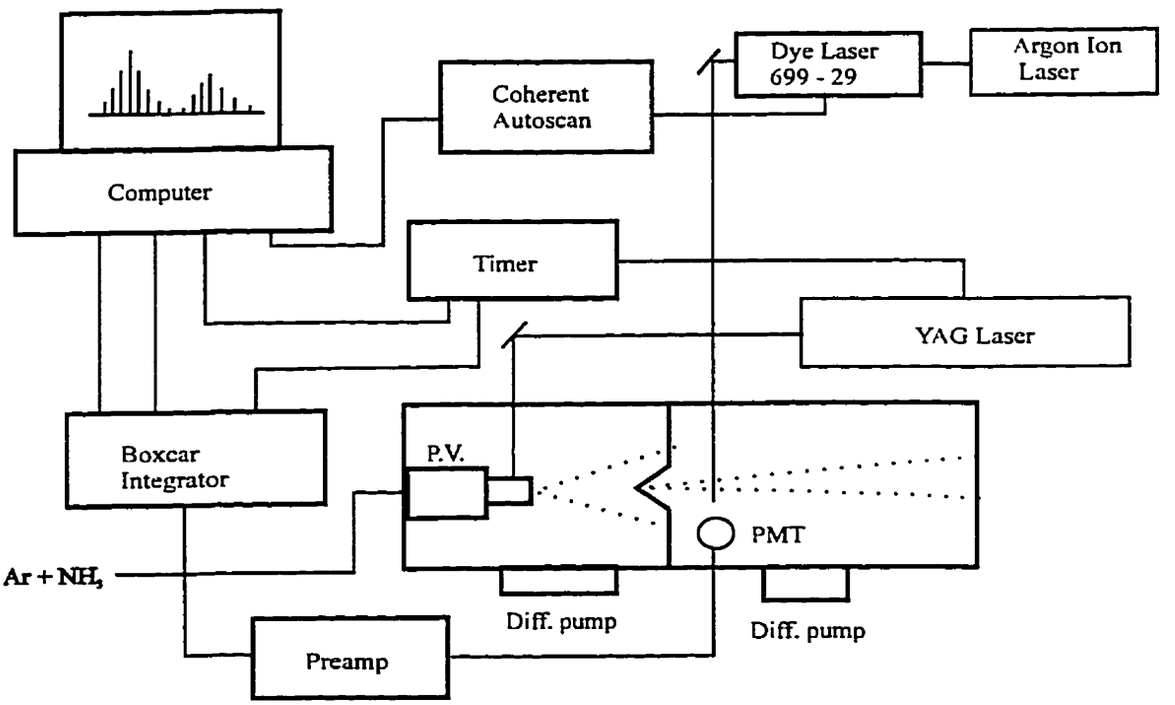

Figure 2.1 Experimental Setup

2.2 Sample preparation and reactant addition

As mentioned in the previous section, laser vaporization can be used to produce an intense pulsed plume of atoms of virtually any element in the periodic table, and by combining this technique with supersonic cooling of the vaporized material in an adiabatic expansion, a variety of cold clusters and cluster ions can be produced (13-15). The vaporization of the solid target is performed inside the throat of a pulsed valve.

Because of the high power density of the laser, a hole will be drilled in the target surface very quickly if the laser is kept at the same spot, and this hole will enclose the vapor cloud. In order to obtain stable shot-to-shot production of atoms the target should move to renew the target continuously. In our apparatus, a metal rod (1/4" in diameter for Ca, 3/8" for Sr) was used as the target, and a synchronous AC motor (3 RPM) was used to drive a micrometer screw to rotate and translate the rod in the nozzle (Figure 2.2). In this way the vaporizing laser can hit a fresh part of the target at every shot. Reasonably good shot-to-shot stability was obtained in our apparatus. A 24 V General Valve solenoid pulsed valve with a nozzle diameter of 0.8 mm was used to produce the molecular beam. The rod holder has a expansion channel of about 1 mm in diameter and 10 mm in length plus a 4 mm long cone shaped nozzle. A 1 mm hole was drilled perpendicular to the expansion channel so that the YAG laser can hit the surface. The metal rod side of the channel was machined in such a way that metal rod protrudes into

the channel a little bit when it was tightly held against the rod holder. In this way the expanding gas can efficiently pick up the metal vapor. An extra pusher was added to push the metal rod tightly against the channel wall. The YAG laser beam was focused on to the metal surface to give a 1 mm diameter spot. The laser pulse energy at 532 nm was about 100 mJ (1 W at 10 Hz) when the flashlamp discharge voltage was set to about 1.35 - 1.4 kV. If a higher laser power was used then the signal-to-noise ratio decrease substantially.

This technique has been used to form a variety of diatomic and polyatomic molecules. Accidentally, the presence of unknown amounts of impurity in the target led the to production and detection of several oxides (16,17), hydrides (17.9). mixed nuclear clusters (18) and polyatomic molecules (19, 9). Alloys were also vaporized to

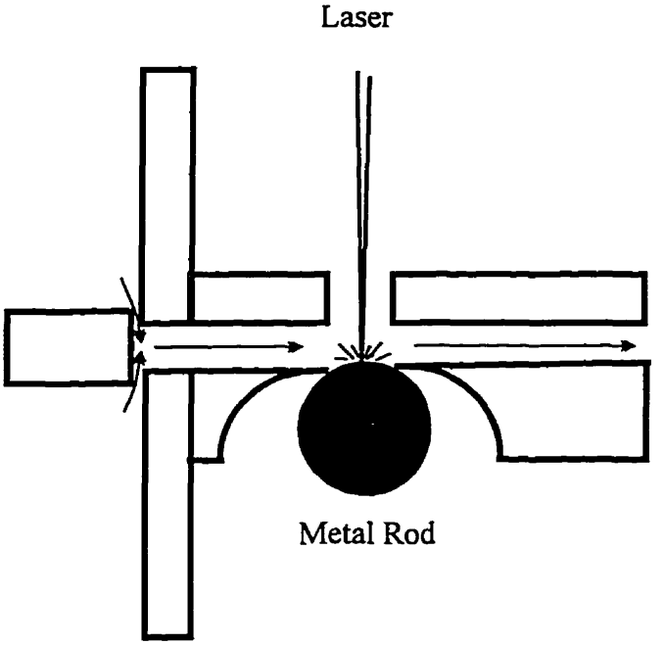

Figure 2.2 Laser Ablation Assembly

generate mixed metal cluster beams (20, 3). Addition of a reactant gas to the carrier gas expanded through the pulsed valve yielded a new method for the production of a large number of different molecules. In this reactive laser vaporization, highly excited species in the laser-generated plasma react more readily with some of the molecules than when they are in the ground state. This fact is illustrated by experiments performed in a Broida

oven, in which a second laser was used to excite Ca or Sr atoms to higher electronic states, and this improved the production of product molecules typically by a factor of 10^3.

In our experiment He and Ar were used as carrier gases and D_2O, NH_3 and $HOCH_3$ as the reactants. When He was used the molecules were cooled down to about 200 K and a much lower temperature of about 10 K was achieved when Ar was used.

2.3 Cooling of the supersonic expansion

The initial stage of the adiabatic expansion from the nozzle orifice is very important for the final composition of the molecular beam. The shape and the length of the expansion channel strongly influences the flow characteristics and hence the mixing of the gas with the vaporized material. Longer expansion channels, both conical and cylindrical, have been shown to lead to extensive cluster formation (21-23) and can be used to intentionally reheat the supersonic jet to a desired rotational temperature (24). Therefore shorter and wider flow channels should be used whenever condensation has to be avoided (25 - 27) and very low rotational temperatures are required.

For a Boltzmann distribution at room temperature, many high J rotational levels are occupied and, for some larger molecules, even excited vibrational levels can be occupied. Excitation from these numerous energy levels to a higher electronic state results in a large number of transitions and possible overlapping of lines in the spectrum. This can make the spectrum too complicated to analyse. By using the supersonic molecular beam

technique, the internal energy of the molecules can be decreased so that only the ground vibrational level and a few lower J rotational levels are populated. A very simple and clean spectrum is then obtained.

The temperature of the molecules in supersonic beam can be determined by analyzing the intensity of the lines in the the spectrum. Studies have shown that diatomic molecules can be cooled to translational, vibrational, and rotational temperatures below 5 K, 100 K and 10 K, respectively (13). The actual temperatures will depend on the nature of the carrier gas, gas pressure, nozzle diameter and the vaporized material. The following formula can be used to determine the rotational temperature (28):

$$\log(I_{em}/(J' + J'' +1)) = A - B_v J'(J' + 1)hc/kT \qquad (2.1)$$

where A can be considered as a constant, I_{em} is the intensity of the transitions, J′ and J″ are the ground and excited state rotational quantum numbers, respectively, and B_v is the rotational constant. If the left side of eq. 2.1 is plotted against J′(J′ + 1) then the slope will give the rotational temperature. Our estimation for the rotational temperature of $CaNH_2$ is below 10 K in Ar.

2.4 Sub-Doppler laser excitation spectroscopy

Sub-Doppler detection is another advantage of the molecular beam technique. By crossing the probe laser and the molecular beam at right angles, Doppler broadening can be reduced and very high resolution obtained. The divergence of the molecular beam limits the resolution that can be achieved.

At room temperature, the Doppler broadening for $CaNH_2$ is about 1 GHz full width at half maximum. The estimate of the residual Doppler broadening for our system is about 180 MHz, which agrees with the experimental line width of 200 MHz.

Figure (2.3) is a schematic diagram of the beam source and the LIF detection assembly. The PMT is placed at right angles to both the molecular beam and the probe laser. A lens assembly is used to enhance the LIF collection efficiency Figure (2.4). The first lens in front of the probe region has a focal length of 1.5" and the second lens has a focal length of 7". The position of the first lens is adjustable to collimate the laser-induced fluorescence. The PMT can be moved to make sure that fluorescence is centered on the PMT photocathode. To reduce the amount of scattered light, a plate with a 5 mm aperture is placed between the two lenses. The PMT is placed inside a thermoelectrically cooled chamber, made by Products for Research, in order to reduce the dark counts. A lens with a focal length of 1 m was used to focus the dye laser beam to a spot about 2 mm in diameter at the probe region. The laser power is about 30 mW.

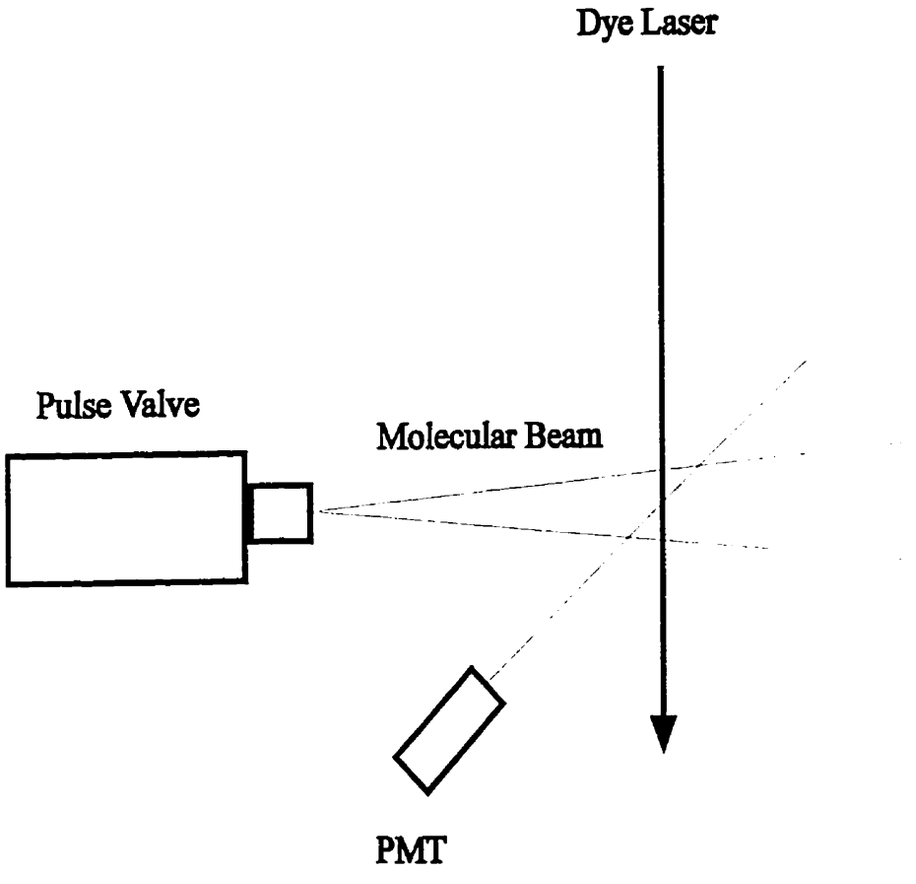

Figure 2.3 Sub-Doppler Detection

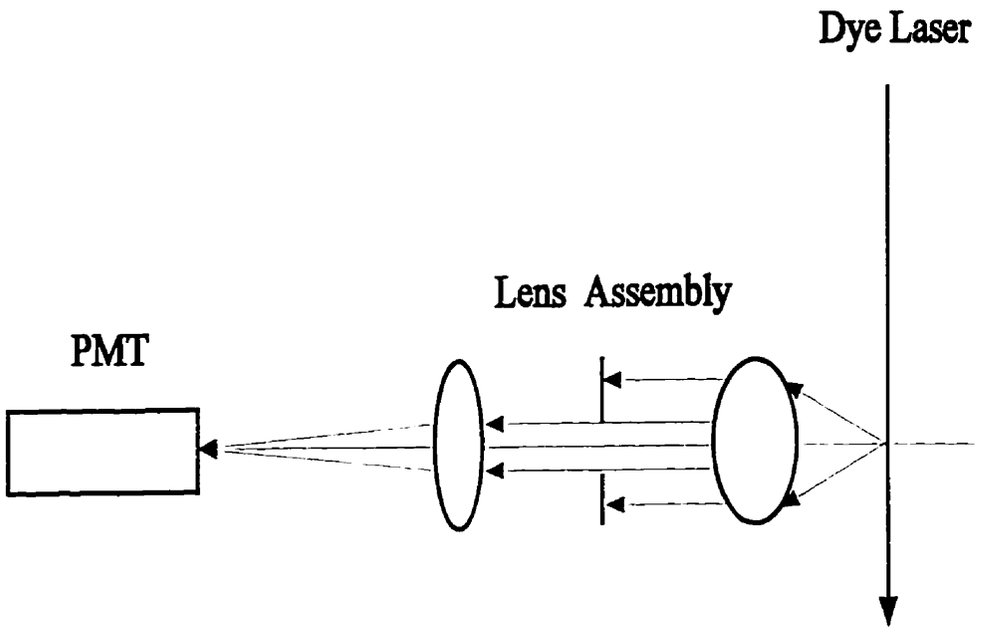

Figure 2.4 LIF Detection Assembly

2.5 Control electronics and data acquisition

Figure (2.5) shows a block diagram of the control electronics of the spectrometer. Trigger pulses at 10 Hz generated by the computer are used to trigger a home-made timing control box which then triggers the pulsed valve driver, YAG laser and boxcar integrator at the appropriate delay times. The timing sequence is shown in Figure (2.6).

The 0.3 ms gas pulse will appear after a 0.55 ms time delay from the triggering of the pulsed valve driver. At this instant, the Q-switch of the YAG laser is opened and the ablation takes place at the leading edge of the gas pulse. The molecules then travel for about 0.2 ms down to the probing region (when Ar is used), and a time window of 40 μs is opened by the boxcar intergrator to collect the LIF signal. The output of the boxcar is sent to the Coherent Autoscan computer to record the spectrum.

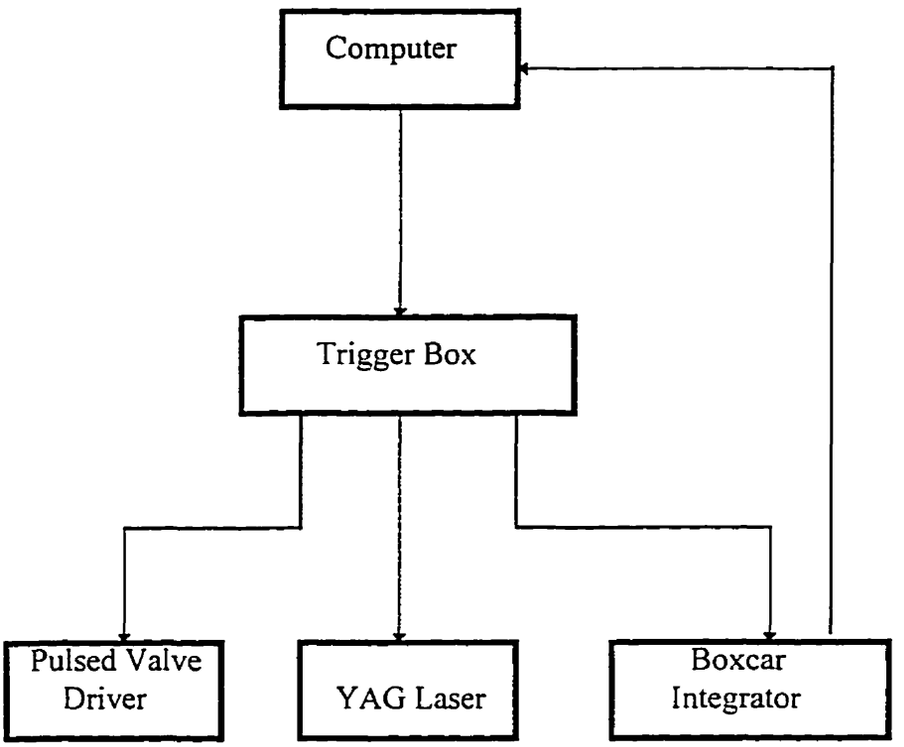

Figure 2.5 Block Diagram for Control Electronics

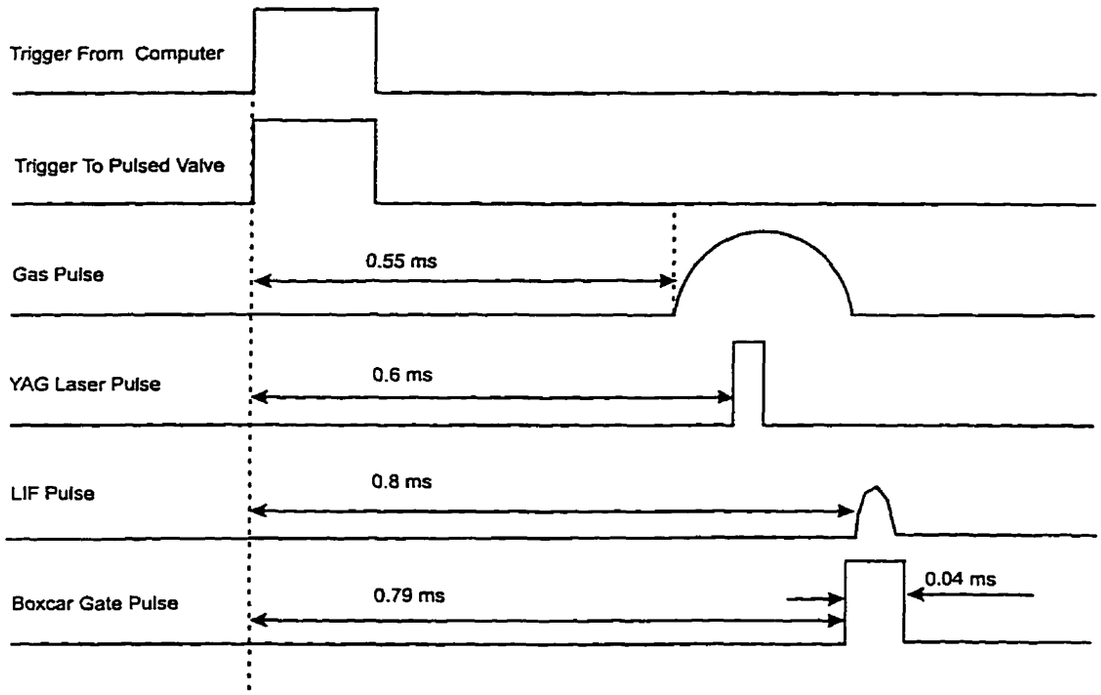

Figure 2.6 Timing Sequence for the System

2.6 References

1. R.A. Bingham and P.L. Salter, Anal. Chem. 48, 1735 (1976).
2. H. Kang and J.L. Beauchamp, J. Phys. Chem. 89, 3364 (1985).
3. R.G. Wheeler, K. LaiHing, W.L. Wilson, J.D. Allen, R.B. King and M.A. Duncan, J. Am. Chem. Soc. 108, 8101 (1986).
4. V.E. Bondybey and J.H. English, J. Chem. Phys. 76, 2165 (1982).
5. L.J. Radziemski, R.W. Solarz and J.A. Paisner, Optical engineering, vol 11: Laser spectroscopy and its applications, Marcel Dekker Inc., New York.
6. D.I. Rosen, J. Mitteldorf, D. Kothandaraman, A.N. Pirri and E.R. Pugh, J. Appl. Phys. 53, 3190 (1982).
7. J.T. Knudtson, W.B. Green and D.G. Sutton, J. Appl. Phys. 61, 4771 (1987).
8. J.F. Fruchtenicht, Rev. Sci. Instr. 45, 51 (1971).
9. V.E. Bondybey, Science 227, 125 (1985).
10. M.E. Geusic, M.D. Morse, S.C. O'Brien and R.E. Smalley, Rev. Sci. Instr. 56, 2123 (1985).
11. P.J. Brucat, L.S. Zheng, C.L. Pettiette, S. Yang and R.E. Smalley, J. Chem. Phys. 84, 3078 (1986).
12. B.G. Wicke, S.P. Tang and J.F. Fruchtenicht, Chem. Phys. Lett. 53, 304 (1978).
13. D.E. Powers, S.G. Hansen, M.E. Geusic, A.C. Puluz, J.B. Hopkins,

T.G. Dietz, M.A. Duncan, P.R.R. Langridge-Smith and R.E. Smalley,
J. Phys. Chem. 86, 2556 (1982).

14. V.E. Bondybey and J.H. English, J. Chem. Phys. 74. 6978 (1981).
15. E.A. Rohlfing, D.M. Cox and A. Kaldor, J. Chem. Phys. 81, 3322 (1984).
16. E.A. Rohlfing, D.M. Cox and A. Kaldor, Chem. Phys. Lett. 99, 161 (1983).
17. M.F. Cai, T.P. Dugan and V.E. Bondybey, Chem. Phys. Lett. 155, 430 (1989).
18. V.E. Bondybey and J.H. English, J. Chem. Phys. 79, 4746 (1983).
19. T.G. Dietz, M.A. Duncan, D.E. Powers and R.E. Smalley,
J. Chem. Phys. 74, 6511 (1981).
20. V.E. Bondybey, G.P. Schwartz and J.H. English, J. Chem. Phys.78, 11 (1983).
21. Y. Lin, Q. Zhang, F.K. Tittel, R.F. Curl and R.E. Smalley,
J. Chem. Phys. 85, 7437 (1986).
22. D.M. Cox, K.C. Reichmann and A. Kaldor, J. Chem. Phys. 88, 1588 (1988).
23. C.L. Callender, S.A. Mitchell and P.A. Hackett, J. Chem. Phys. 90, 2535 (1989).
24. D.L. Michalopoulos, M.E. Geusic, P.R.R. Langridge-Smith and R.E. Smalley,
J. Chem. Phys. 80, 3556 (1984).
25 M. Ebben, G. Meijer and J.J. ter Meulen, Appl. Phys. B 50, 35 (1990).
26 J. M. Gardner and M.I. Lester, Chem. Phys. Lett. 137, 301 (1987).
27. M. Costes, C. Noulin, G. Dorthe, C. Vaucanmps and G. Nouchi,
Farad. Disc. Chem. Soc. 84, 75 (1987).
28. G. Herzberg, Spectra of Diatomic Molecules, Van Nostrand, N.Y., pg. 205

CHAPTER 3

HIGH RESOLUTION LASER EXCITATION SPECTROSCOPY OF THE $\tilde{B}^2\Sigma^+$- $\tilde{X}^2\Sigma^+$ SYSTEM OF JET-COOLED SrOD

3.I Introduction

In recent years there has been a surge of interest in the alkaline earth monohydroxide molecules. For SrOH and SrOD, the pioneering work was the rotational analysis of the 000-000, 001-001 and 010-010 bands of the $\tilde{B}^2\Sigma^+ - \tilde{X}^2\Sigma^+$ transition by Nakagawa, Wormsbecher and Harris in 1983 (1). Since then the 000-000 band of the $\tilde{A}^2\Pi - \tilde{X}^2\Sigma^+$ transition of SrOH has been analysed (2), followed by work on additional bands of the $\tilde{A} - \tilde{X}$ (3) and $\tilde{B} - \tilde{X}$ (4) transitions. Microwave (5) and millimeter wave (6,7) spectra of SrOH are available and the dipole moments in the $\tilde{X}$, $\tilde{A}$ and $\tilde{B}$ states were determined from the Stark effect in a molecular beam (8). Semi-empirical calculations based on a modified Rittner model (9) and ligand field theory (10) have been used to predict energy levels and dipole moments.

The previous spectrum of SrOD was recorded in a Broida oven (1) so that the resolution was limited by Doppler broadening and weak Q-branch lines were not seen. In a supersonic jet expansion the molecules are vibrationally and rotationally cooled in order

to simplify the spectrum. The molecular beam is crossed at right angles with a laser beam so that sub-Doppler spectra are obtained.

The 000-000 and 001-000 bands of the $\widetilde{B}\,^2\Sigma^+ - \widetilde{X}\,^2\Sigma^+$ system of SrOD were studied in our work. The $\widetilde{A}\,^2\Pi_{1/2}$ and $\widetilde{B}\,^2\Sigma^+$ states are mixed by off-diagonal spin-orbit coupling. The $\widetilde{B}\,^2\Sigma^+ - \widetilde{X}\,^2\Sigma^+$ transition is nominally a parallel transition which should have very weak Q branches which decrease rapidly in intensity as J increases. However, the $\widetilde{A}\,^2\Pi_{1/2}$ ~ $\widetilde{B}\,^2\Sigma^+$ mixing induces some perpendicular character in the $\widetilde{B} - \widetilde{X}$ transition and enhances the intensity of the Q branches. By comparing the intensities of the P, Q and R branches it is possible to deduce the ratio of the parallel to the perpendicular transition dipole moment.

With the exception of the millimeter wave work (6) on SrOD, all of the recent studies have concentrated on SrOH. We report here on the analysis of the 001-000 and 000-000 bands of SrOD, recorded in order to test the new laser ablation spectrometer.

3.2. Experimental

The experimental apparatus was described in detail in chapter 2. However, some of the specific conditions used are listed here. The supersonic molecular beam was produced by a home-made piezo-driven pulsed valve and collimated by a 3 mm diameter stainless

steel skimmer located 3 cm from the nozzle (5,8). The second harmonic (532 nm) of a 10 Hz pulsed Nd/YAG laser was used to vaporize the metal. The beam was formed by expansion of 2.7 atm of helium flowing over liquid D_2O. A Sr metal rod with a 5 mm diameter was rotated and translated during the experiment. The ablation laser was weakly focused onto the sample and entered the sample holder through a 1 mm hole. The expansion channel is about 1 mm in diameter and 10 mm long.

Kiton red dye was used in the Coherent 699-29 dye laser at a wavelength of about 620 nm. A band pass filter (40 nm) centered at the laser frequency was used for the 000–000 transition. When recording the 001 - 000 band, a band pass filter (40 nm) centered on the 001–001 transition and a red pass filter were used, and in this way a much better signal-to-noise ratio was obtained. A time "window" of 20 μs was opened by the boxcar integrator after a 100 μs delay from when the ablation laser fired. To increase the signal-to-noise ratio, the ring dye laser was set in continuous mode and at least five pulses were averaged for each frequency point. Therefore, 100 s was needed for each 10 GHz scan using 50 MHz steps.

3.3. Results and Discussion

Spectroscopic studies of the monovalent alkaline earth derivatives show that a simple one electron hydrogenic picture can provide a reasonable model of the electronic structure.

Sr^+OD^- can be considered to be an ionic molecule like CaF (Figure 3.1). SrOD is linear, rather than bent like H_2O or CaSH, because there is a partial positive charge on the deuteron of the OD^- group. The linear geometry maximizes the distance between the Sr^+ unit and the deuteron. As the ligand becomes less electronegative, the degree of covalency in the metal-ligand bond increases and the molecule is bent rather than linear, such as CaSH.

The neutral Sr atom has a $[Kr]5s^2$ electronic configuration and when Sr^+OD^- forms, one electron is transferred to the OD ligand. The remaining 5s valence electron on Sr^+ is nonbonding and makes the $\tilde{X}^2\Sigma^+$ ground state of SrOD. The first and second excited states of Sr^+ result from promotion of the 5s electron to 4d and 5p states. The $\tilde{A}^2\Pi$ and $\tilde{B}^2\Sigma^+$ states of SrOD originate from the pπ and pσ orbitals correlating with the 5p Sr^+ orbital mixed with the dπ and dσ orbitals correlating with the 4d Sr^+ orbital.The $\tilde{B}^2\Sigma^+$ and $\tilde{A}^2\Pi$ states are pσ-dσ and pπ-dπ orbital mixtures polarized to keep the unpaired electron as far away from the OD^- group as possible.

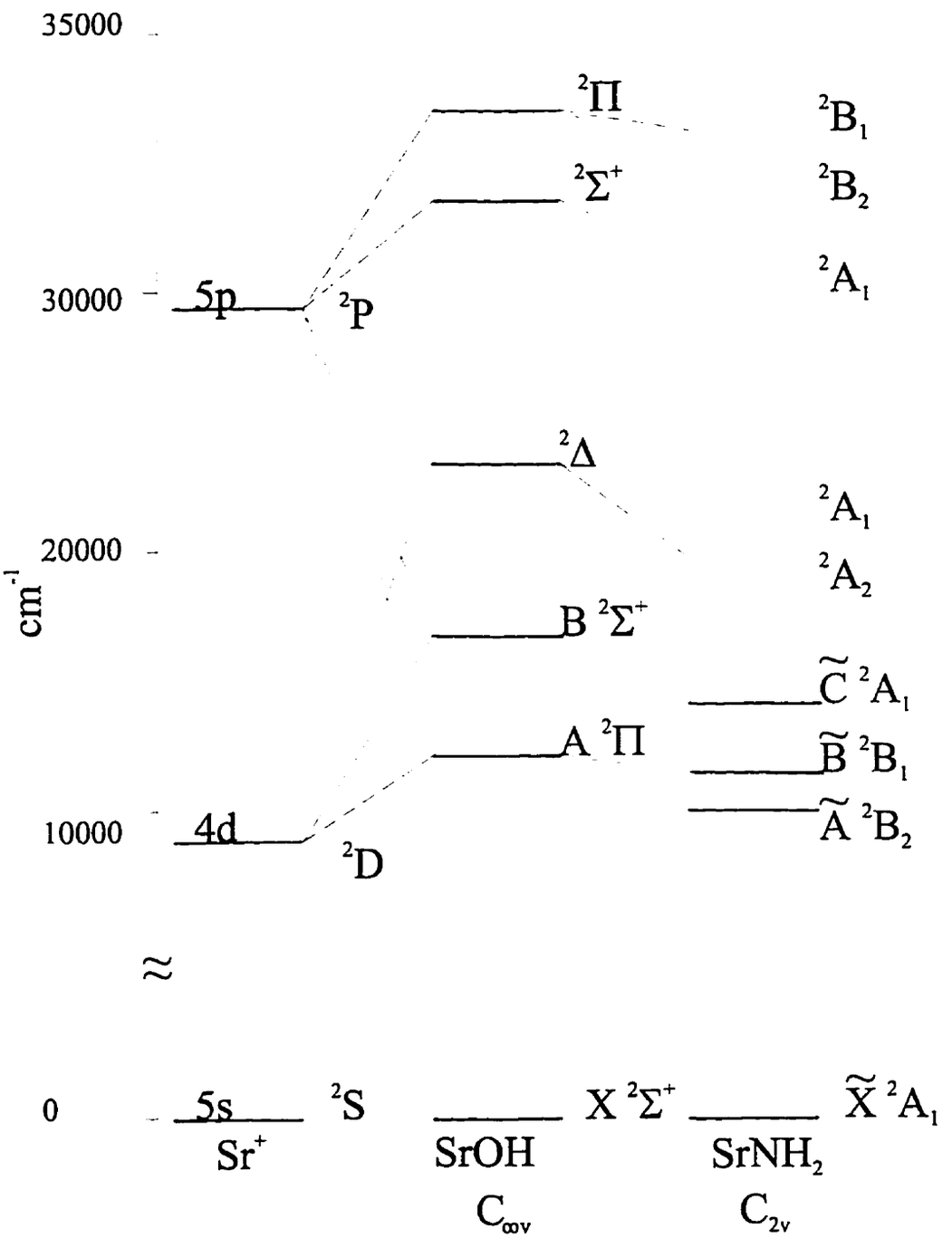

Figure 3.1 Energy Level Correlation Diagram

The 001–000 and 000–000 bands of the $\widetilde{B}^2\Sigma^- - \widetilde{X}^2\Sigma^+$ transition of SrOD were rotationally analyzed. The $^2\Sigma^+$ states of SrOD adopt Hund's case (b) coupling (Figure 3.2). As always, the total angular momentum J is a good quantum number, however, the rotational angular momentum N also becomes good quantum number. The rotational energy levels can be approximated by:

$$E_{rot} = B_v N(N+1) \qquad (3.1)$$

where N = 0, 1, 2, ... The total angular momentum quantum number can be derived from N and the spin quantum number S (=1/2) by:

$$J = N + 1/2, N - 1/2 \qquad (3.2)$$

for a $^2\Sigma$ state.

For Hund's case (b) , the selection rules are $\Delta N = \pm 1$. For a $^2\Sigma$ state, each rotational energy level is split into two spin components: $J = N + S = N + 1/2$ for F_1 and $J = N - S = N - 1/2$ for F_2. The selection rule for J is $\Delta J = 0, \pm 1$, so that P and R branchs and satellite Q branch lines should appear for each spin component. Figure 3.3 shows the possible branches for a $^2\Sigma$ - $^2\Sigma$ transition.

The analysis of the spectra was straightforward with the help of the previous work (1). As a result of rotational cooling, the first few lines and the band origin were easily located (Figure 3.4). The line positions of the two bands were measured with a program called Decomp and are reported in Tables 3.1 and 3.2.

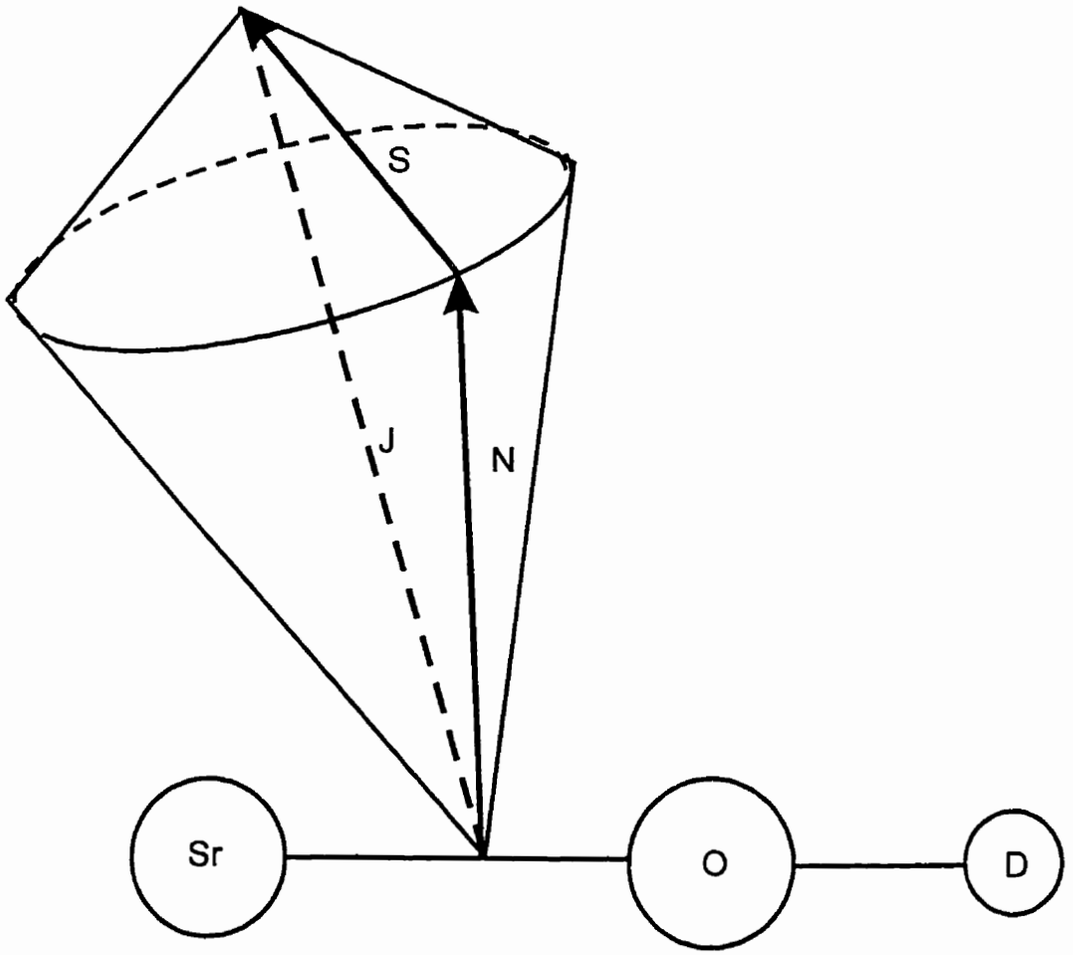

Figure 3.2 The Angular Momentum Coupling Diagram for Hund's Case (b)

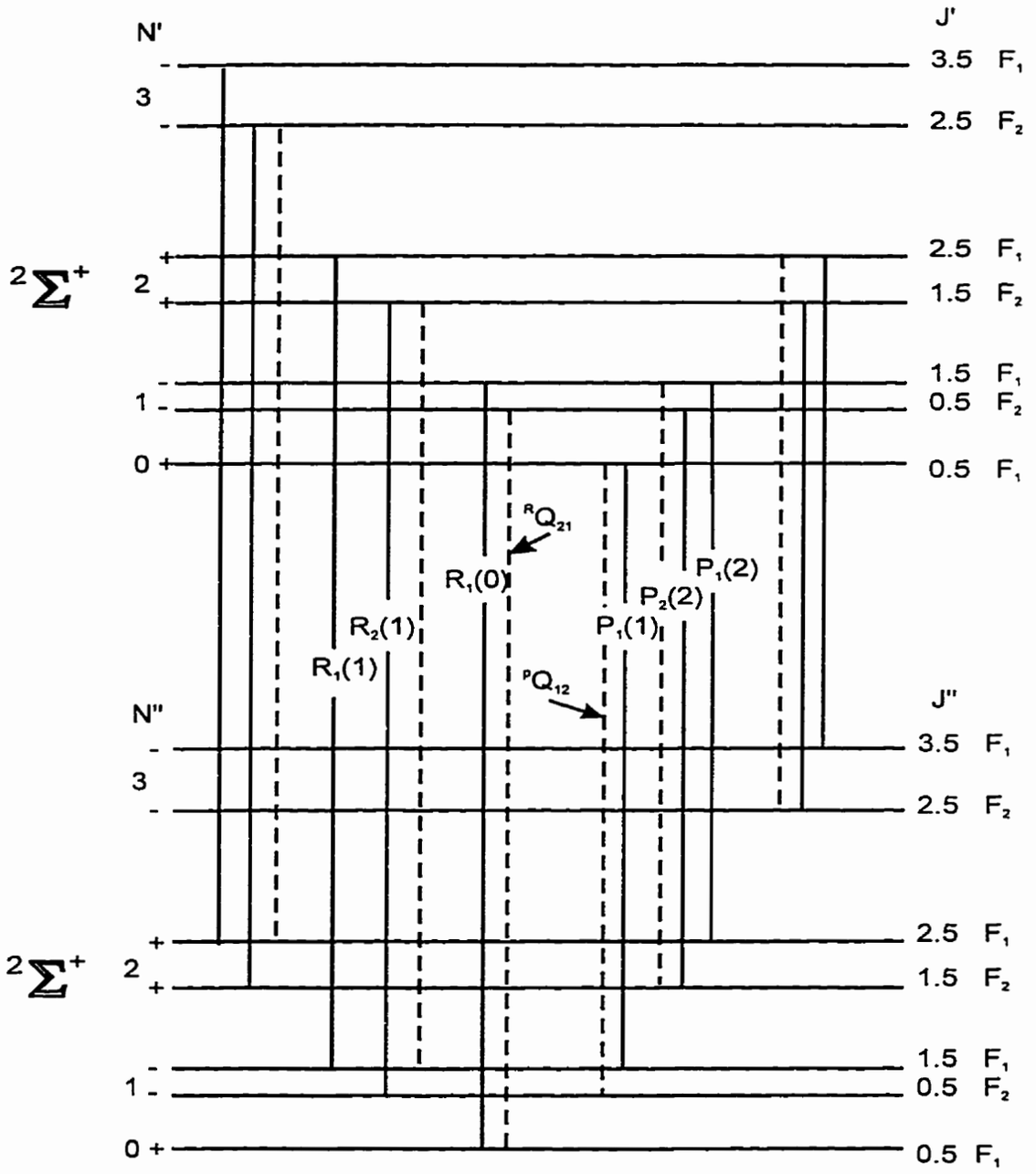

Figure 3.3 Energy Level Diagram for $^2\Sigma^+$ - $^2\Sigma^+$ Transition

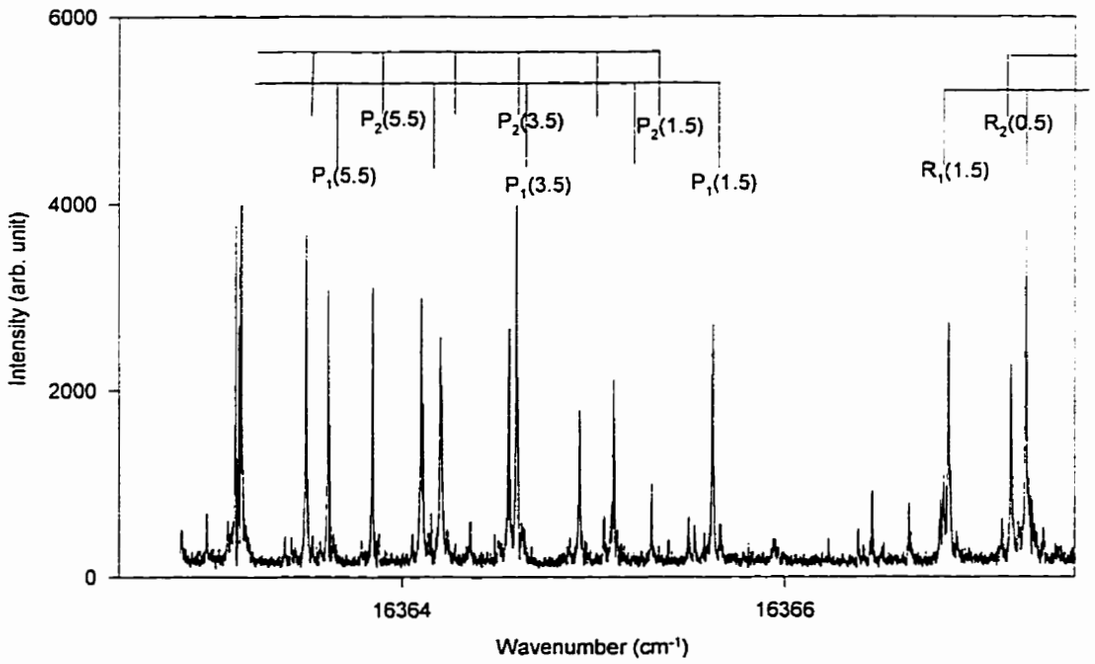

Figure 3.4 A Portion of the High-Resolution Spectrum Showing P and R Branches of the 000 - 000 Band of the $\widetilde{B}\,^2\Sigma^+ - \widetilde{X}\,^2\Sigma^+$ Transition of SrOD

The line positions were fitted using the standard N^2 Hamiltonian evaluated using Hund's case (a) basis functions (12). The $^2\Sigma$ Hamiltonian (14) can be written as

$$\hat{H} = \hat{H}_{el} + \hat{H}_{so} + \hat{H}_{sr} + \hat{H}_{rot} \qquad (3.2)$$

where the $\hat{H}_{el}$ is the electronic-vibrational Hamiltonian (not including the nuclear kinetic energy term). The spin-orbit part of the Hamiltonian $\hat{H}_{so}$ is given by,

$$\hat{H}_{so} = A(r)\bar{L} \bullet \bar{S} \qquad (3.3)$$

the spin-rotation interaction is,

$$\hat{H}_{sr} = \bar{N} \bullet \bar{S}(\gamma + \gamma_D \hat{N}^2 + \gamma_H \hat{N}^4 + \gamma_L \hat{N}^6) \qquad (3.4)$$

and the rotational part of the Hamiltonian is defined by,

$$\hat{H}_{rot} = B(r)\bar{N}^2 - D(r)\bar{N}^4 + H(r)\bar{N}^6 \qquad (3.5)$$

where

$$\bar{N} = \bar{J} - \bar{S} \qquad (3.6)$$

The Hund's case (a) basis functions were used to derive matrix elements of the standard $^2\Sigma$ hamiltonian, because it is more difficult to obtain the matrix elements with Hund's case (b) basis functions. The case (a) basis function is,

$$| n\upsilon\Lambda S\Sigma \rangle | \Omega J \rangle = | n\upsilon\Lambda S\Sigma\Omega J \rangle \qquad (3.7)$$

where n represents the electronic quantum number, υ is the vibrational quantum number, Σ = S, S-1, ... -S and $\Omega = \Lambda + \Sigma$ (4.48). The two basis functions for a $^2\Sigma$ state are ,

$$| n, \upsilon, \Lambda=0, S=1/2, \Sigma=+1/2, \Omega=+1/2, J \rangle = | {}^2\Sigma_{1/2} \rangle \qquad (3.8)$$

$$| n, \upsilon, \Lambda=0, S=1/2, \Sigma=-1/2, \Omega=-1/2, J \rangle = | {}^2\Sigma_{-1/2} \rangle \qquad (3.9)$$

and they can be transformed into the following form to diagonalize the 2x2 Hamiltonian matrix,

$$| {}^2\Sigma_{1/2}(e) \rangle = (| {}^2\Sigma_{1/2} \rangle + | {}^2\Sigma_{-1/2} \rangle)/\sqrt{2} \qquad (3.10)$$

$$| {}^2\Sigma_{1/2}(f) \rangle = (| {}^2\Sigma_{1/2} \rangle - | {}^2\Sigma_{-1/2} \rangle)/\sqrt{2} \qquad (3.11)$$

where *e* and *f* are parity basis functions. The Hamiltonian matrix elements in the transformed basis set are listed in the Table 3.3.

The 001–000 and 000–000 bands, and the pure rotational transitions (6) were fitted together to provide the constants of Table 3.4. A small perturbation was noted in the excited state F_2 component of the 001 $\tilde{B}\,{}^2\Sigma^+$ state close to N' = 14, J' = 13.5, f parity (Table II). These lines were included with reduced weights in the final fit.

For pure ${}^2\Sigma^+ - {}^2\Sigma^+$ transitions, Q branches are forbidden . If there is ${}^2\Pi_{1/2}$ character mixed into a ${}^2\Sigma^+$ state then the intensity of the Q branches is enhanced. Figure 3.5 shows the well resolved Q branch lines in the P branch region. Kopp and Hougen (13) considered the intensity of the branches of a general 1/2–1/2 transition and derived the following formulas:

$$P_{ee}:[(J+1/2)(J-1/2)/J][\,\mu_{||} - \mu_{\perp}]^2 \qquad (3.12)$$

$$Q_{ef}:[2(J+1/2)^3/J(J+1)][\,\mu_{||}/(2J+1) - \mu_{\perp}]^2 \qquad (3.13)$$

Application of these expressions to the 000–000 band gives a ratio of $\mu_\perp/\mu_{||}$ of about 0.2 to 0.3 for the $\widetilde{B}\,^2\Sigma^+ - \widetilde{X}\,^2\Sigma^+$ transition of SrOD. The 001–000 band is weaker than the 000–000 band so that Q branches were not detected. The value of the Sr - O stretching mode frequency, ν_3, in the $\widetilde{B}\,^2\Sigma^+$ state of SrOD is found to be 523.652 cm^{-1} by subtraction of the band origins. The use of our 001-000 band origin and Nakagawa et al.'s (1) 001-001 band origin of 16372.6281, gives a value of 517.122 cm^{-1} for ν_3 in the $\widetilde{X}\,^2\Sigma^+$ state.

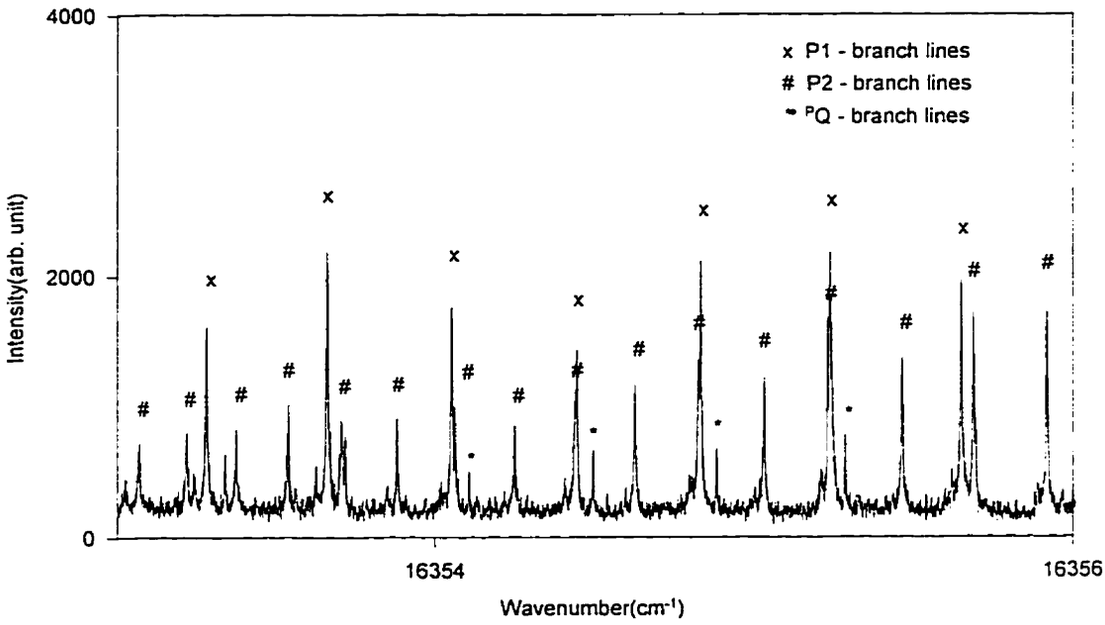

Figure 3.5 A Portion of the P Branch of the 000 - 000 Band of the $\widetilde{B}\,^2\Sigma^+ - \widetilde{X}\,^2\Sigma^+$ Transition of SrOD Showing Q-Branch Lines

Table 3.1. Line positions (in cm^{-1}) for the $\widetilde{B}\,^2\Sigma^+(000)$-$\widetilde{X}\,^2\Sigma^+(000)$ band of SrOD. The table shows ν_{obs}, and the residuals, ν_{obs}-ν_{calc}

N	P_1	
2	16365.6515	0.0049
3	16365.1368	0.0012
4	16364.6325	0.0025
5	16364.1319	0.0022
6	16363.6358	0.0011
7	16363.1454	0.0002
8	16362.6730	0.0120
9	16362.1860	0.0038
10	16361.7160	0.0072
11	16361.2490	0.0082
12	16360.7807	0.0025
13	16360.3263	0.0054
14	16359.8694	0.0003
15	16359.4225	-0.0000
16	16358.9821	0.0005
17	16358.5450	-0.0008
18	16358.1183	0.0026
19	16357.7631	0.0022
20	16357.2724	0.0009
21	16356.8597	0.0022
22	16356.4514	0.0025
23	16356.0460	0.0003
24	16355.6511	0.0031
25	16355.2554	-0.0006
26	16354.8695	0.0007
27	16354.4889	0.0015
28	16354.1127	0.0013
29	16353.7405	-0.0002
30	16353.3757	0.0000
31	16353.0151	-0.0008
32	16352.6616	-0.0001
33	16352.3105	-0.0024
34	16351.9696	0.0000
35	16351.6309	-0.0007
36	16351.2959	-0.0032
37	16350.9717	-0.0004
38	16350.6488	-0.0018
39	16350.3352	0.0006
40	16350.0248	0.0009
41	16349.7189	0.0001
42	16349.4194	0.0004
43	16349.1239	-0.0008
44	16348.8379	0.0019
45	16348.5538	0.0011
46	16348.2736	-0.0011
47	16348.0040	0.0016
48	16347.7337	-0.0017
49	16347.4732	-0.0007
50	16347.2210	0.0030
N	R_1	
2	16366.8911	0.0058
3	16367.2867	0.0005
4	16367.6962	0.0037
5	16368.0986	-0.0054
6	16368.5166	-0.0044
7	16368.9412	-0.0021
8	16369.3697	-0.0012
9	16369.7975	-0.0063
10	16370.2804	0.0383
11	16370.6845	-0.0010
12	16371.1310	-0.0034
13	16371.5808	-0.0077
14	16372.0461	-0.0018
15	16372.5094	-0.0033
16	16372.9814	-0.0013
17	16373.4537	-0.0043
18	16373.9390	0.0004
19	16374.4237	-0.0006
20	16374.9158	0.0003
21	16375.4129	0.0010
22	16375.9137	0.0002
23	16376.4195	-0.0007
24	16376.9314	-0.0009
N	P_2	
2	16365.3374	0.0024
3	16364.9629	0.0021
4	16364.5934	0.0014
5	16364.2346	0.0060
6	16363.8732	0.0027
7	16363.5160	-0.0017
8	16363.1736	0.0031
9	16362.8390	0.0105
10	16362.5110	0.0190
11	16362.1860	0.0252
12	16361.8380	0.0030
13	16361.5230	0.0083
14	16361.1990	-0.0006
15	16360.9060	0.0159
16	16360.5886	0.0027

Table 3.1 (Continued)

17	16360.2904	0.0032
18	16359.9958	0.0020
19	16359.7084	0.0025
20	16359.4225	-0.0008
21	16359.1490	0.0028
22	16358.8720	-0.0025
23	16358.6072	-0.0010
24	16358.3487	0.0012
25	16358.0881	-0.0039
26	16357.8424	0.0003
27	16357.6000	0.0024
28	16357.3595	0.0010
29	16357.1239	-0.0008
30	16356.8976	0.0010
31	16356.6756	0.0017
32	16356.4513	-0.0051
33	16356.2453	0.0007
34	16356.0459	0.0077
35	16355.8376	0.0004
36	16355.6510	0.0093
37	16355.4537	0.0021
38	16355.2655	-0.0014
39	16355.0861	-0.0017
40	16354.9255	0.0114
41	16354.7461	0.0002
42	16354.5834	0.0003
43	16354.4190	-0.0067
44	16354.2740	0.0001
45	16354.1237	-0.0038
46	16353.9873	0.0007
47	16353.8500	-0.0011
48	16353.7222	0.0010
49	16353.5959	-0.0007
50	16353.4793	0.0017

N	R_2	
1	16367.2098	-0.0019
2	16367.7458	0.0016
3	16368.2786	-0.0032
4	16368.8216	-0.0033
5	16369.3697	-0.0036
6	16369.9241	-0.0030
7	16370.4832	-0.0030
8	16371.0474	-0.0031
9	16371.6139	-0.0063
10	16372.1926	-0.0026
11	16372.7728	-0.0028
12	16373.3592	-0.0020
13	16373.9506	-0.0015
14	16374.5508	0.0025
15	16375.1461	-0.0036
16	16375.7562	-0.0003
17	16376.3689	0.0003
18	16376.9853	-0.0005

N	Q_{1ef}	
12	16360.3522	0.0038
13	16359.9025	0.0037
14	16359.4536	-0.0008
15	16359.0171	0.0014
16	16358.5822	0.0000
17	16358.1572	0.0030
18	16357.7332	0.0016
20	16356.8977	-0.0048
21	16356.4990	0.0028
22	16356.0958	0.0006
23	16355.7032	0.0035
24	16355.3101	0.0005
25	16354.9256	0.0007
26	16354.5472	0.0015
27	16354.1728	0.0009
28	16353.8020	-0.0015
29	16353.4401	-0.0004
30	16353.0827	-0.0003
31	16352.7305	-0.0005
32	16352.3793	-0.0051
33	16352.0425	-0.0007

N	Q_{1fe}	
11	16372.1704	-0.0017
12	16372.7496	-0.0007
13	16373.3324	-0.0013
14	16373.8896	-0.0328
15	16374.5189	0.0025
16	16375.1119	-0.0037
17	16375.7193	-0.0009

Table 3.2 Line positions (in cm^{-1}) for the $\tilde{B}\,^2\Sigma^+(001) - \tilde{X}\,^2\Sigma^-(000)$ band of SrOD. The table shows ν_{obs}, and the residuals, $\nu_{obs}-\nu_{calc}$

N	P_1	
2	16889.3002	0.0014
3	16888.7894	0.0044
4	16888.2777	0.0037
5	16887.7692	0.0034
6	16887.2662	0.0060
7	16886.7579	0.0005
8	16886.2566	-0.0007
9	16885.7600	0.0000
10	16885.2648	-0.0008
11	16884.7716	-0.0022
12	16884.2860	0.0010
13	16883.8036	0.0048
14	16883.3195	0.0042
15	16882.8349	0.0002
16	16882.3551	-0.0016
17	16881.8814	-0.0003
18	16881.4109	0.0014
19	16880.9395	-0.0004
20	16880.4732	-0.0000
21	16880.0088	-0.0005
22	16879.5479	-0.0003
23	16879.0891	-0.0008
24	16878.6323	-0.0021
25	16878.1792	-0.0025
26	16877.7286	-0.0033
27	16877.2818	-0.0031
28	16876.8380	-0.0026
29	16876.3982	-0.0011
30	16875.9611	0.0003
31	16875.5238	-0.0011
32	16875.0904	-0.0016
33	16874.6626	0.0006
34	16874.2339	-0.0009
35	16873.8129	0.0025
36	16873.3874	-0.0014
37	16872.9705	0.0004
38	16872.5524	-0.0018
39	16872.1389	-0.0022
40	16871.7306	-0.0004
41	16871.3221	-0.0015

N	R_1	
1	16890.1375	-0.0015
2	16890.5298	0.0004
4	16891.3161	-0.0018
5	16891.7142	-0.0021
6	16892.1161	-0.0013
7	16892.5228	0.0015
8	16892.9267	-0.0010
9	16893.3393	0.0023
10	16893.7518	0.0029
11	16894.1647	0.0012
12	16894.5799	-0.0008
13	16895.0033	0.0026
14	16895.4258	0.0025
15	16895.8499	0.0013
16	16896.2756	-0.0009
17	16896.7066	-0.0005
18	16897.1420	0.0015
19	16897.5773	0.0009
20	16898.0116	-0.0033
21	16898.4574	0.0012
22	16898.9022	0.0022
23	16899.3456	-0.0008
24	16899.7956	0.0000
25	16900.2476	0.0003
26	16900.7009	-0.0007
27	16901.1586	0.0000
28	16901.6203	0.0021
29	16902.0793	-0.0012
30	16902.5450	0.0000
31	16903.0139	0.0014
32	16903.4854	0.0030
33	16903.9499	-0.0049
34	16904.4309	0.0009
35	16904.9109	0.0033
36	16905.389	0.0011
37	16905.8718	0.0012
38	16906.3546	-0.0013
39	16906.8453	0.0015
40	16907.335	0.0007
41	16907.8275	0.0003
42	16908.3238	0.0011
43	16908.823	0.0023
44	16909.3218	0.0006
45	16909.8225	-0.0016
46	16910.3286	-0.0011

Table 3.2 (Continued)

47	16910.8386	0.0008	1	16890.8550	-0.0014
48	16911.3494	0.0011	2	16891.3769	-0.0041
			3	16891.9081	-0.0003
N	P_2		4	16892.4387	0.0001
2	16888.9835	-0.0012	5	16892.9694	-0.0019
3	16888.6067	0.0012	6	16893.5045	-0.0024
4	16888.2286	-0.0003	7	16894.0394	-0.0057
5	16887.8517	-0.0034	8	16894.5799	-0.0061
6	16887.4815	-0.0025	9	16895.1272	-0.0024
7	16887.1089	-0.0068	10	16895.6681	-0.0078
3	16886.7473	-0.0028	11	16896.2109	-0.0014
9	16886.383	-0.0043	12	16896.7550	-0.0215
10	16886.0206	-0.0067	13	16897.2680	-0.0628
11	16885.6632	-0.0069	14	16897.9202	0.0323
12	16885.3084	-0.0072	15	16898.4574	0.0098
13	16884.9590	-0.0049	16	16899.0203	0.0104
14	16884.5930	-0.0219	17	16899.5835	0.0086
15	16884.2052	-0.0636	18	16900.1508	0.0082
16	16883.9574	0.0319	19	16900.7045	-0.0082
17	16883.6001	0.0152	20	16901.2899	0.0041
18	16883.2610	0.0138	21	16901.8658	0.0045
19	16882.9201	0.0079	22	16902.4432	0.0037
20	16882.5891	0.0091	23	16903.0156	-0.0046
21	16882.2558	0.0052	24	16903.6055	0.0017
22	16881.9275	0.0035	25	16904.1925	0.0027
23	16881.6035	0.0032	26	16904.7808	0.0023
24	16881.2805	0.0012	27	16905.3890	0.0192
25	16880.9627	0.0015	28	16905.9636	0.0000
26	16880.6474	0.0016	29	16906.5614	0.0013
27	16880.3359	0.0026	30	16907.1614	0.0022
28	16880.0243	0.0007	31	16907.7611	0.0003
29	16879.7163	-0.0004	32	16908.3238	-0.0412
30	16879.4122	-0.0005	33	16908.9715	-0.0003
31	16879.1117	0.0001	34	16909.5806	-0.0005
32	16878.8141	0.0009	35	16910.2017	0.0086
33	16878.5174	-0.0002	36	16910.8073	-0.0002
34	16878.2188	-0.0061	37	16911.4256	0.0009
35	16877.9318	-0.0033	38	16912.0424	-0.0018
36	16877.6482	0.0000	39	16912.6662	-0.0001
37	16877.3591	-0.0048	41	16913.9366	0.0183
38	16877.0800	-0.0026	42	16914.5526	0.0046
41	16876.2504	-0.0054	44	16915.8189	0.0039
42	16875.9775	-0.0084			

N	R_2

Table 3.3 Hamiltonian matrix elements for a $^2\Sigma^+$ state using Hund's case (a) parity basis set.

T	*e*	1	γ	*e*	$+0.5\,(J-0.5)$
	f	1		*f*	$-0.5\,(J+1.5)$
B	*e*	$(J+0.5)(J-0.5)$	γ_D	*e*	$+0.5(J-0.5)^2(J+0.5)$
	f	$(J+0.5)(J+1.5)$		*f*	$-0.5(J+1.5)^2(J+0.5)$
D	*e*	$-[(J+0.5)(J-0.5)]^2$	γ_H	*e*	$+0.5(J-0.5)^3(J+0.5)^2$
	f	$-[(J+0.5)(J+1.5)]^2$		*f*	$-0.5(J+1.5)^3(J+0.5)^2$
H	*e*	$[(J+0.5)(J-0.5)]^3$	γ_L	e	$+0.5(J-0.5)^4(J+0.5)^3$
	f	$[(J+0.5)(J+1.5)]^3$		*f*	$-0.5(J+1.5)^4(J+0.5)^3$

Table 3.4
Molecular constants for SrOD (in cm^{-1})

Constant	$\tilde{X}\,^2\Sigma^+(000)$	$\tilde{B}\,^2\Sigma^+(000)$	$\tilde{B}\,^2\Sigma^+(001)$
B	0.22531615(82)	0.227992(24)	0.226681(45)
10^7xD	1.66514(89)	1.6930(46)	1.6833(72)
γ	0.00219960(17)	-0.129270(92)	-0.129510(32)
T_0	-	16366.0983(01)	16889.7505(08)

SrOH and SrOD are linear molecules, therefore, the relationship between the moment of inertia and the bond lengths of a linear molecule can be used to derive the bond lengths,

$$I = (m_1 m_2 r_{12}^2 + m_1 m_3 r_{13}^2 + m_2 m_3 r_{23}^2) / M \qquad (3.14)$$

The moments of inertia for SrOD are calculated from the B values of Table 3.4, while the corresponding data for SrOH was taken from the work of Nakagawa and Harris (1). In this way, the r_0 structures of SrOD in both the $\widetilde{B}\,^2\Sigma^+$ and $\widetilde{X}\,^2\Sigma^+$ states were determined. The results are presented in Table 3.5. The bond lengths of the $\widetilde{B}\,^2\Sigma^+$ state are shorter than those of the $\widetilde{X}\,^2\Sigma^+$ which suggests that the non-bonding valence electron has slight anti-bonding character in the ground state.

Table 3.5 Bond lengths in SrOH and SrOD (in Å).

Bond length	$\widetilde{B}\,^2\Sigma^+$	$\widetilde{X}\,^2\Sigma^+$
r_0(Sr-O)	2.098	2.111
r_0(O-H)	0.921	0.922

3.4 Conclusion

Our high resolution study of SrOD has provided improved molecular constants. This resulted from the cooling of SrOD in a supersonic expansion and sub-Doppler linewidths. The transition wavenumbers were well reproduced with a $^2\Sigma$ Hamiltonian, which proved that SrOD is a linear molecule, consistent with previous work.

The fact that no observable hyperfine splittings were found suggest that the bonding between the metal and the OD group is ionic, M^+OH^-. Studies of other alkaline earth metal hydroxides (6) such as SrOH , CaOH and MgOH support the idea that the metal-OH bonds are mainly ionic in character. Q-branch lines were observed for the first time in the $\widetilde{B}\,^2\Sigma^+$- $\widetilde{X}\,^2\Sigma^+$ transition of SrOD and the ratio of the perpendicular to parallel transition dipole moment was estimated.

3.5 References

1. J. Nakagawa, R.F. Wormsbecher and D.O. Harris, J.Mol.Spectrosc. 97,37(1983)

2. C.R. Brazier and P.F. Bernath, J.Mol.Spectrosc. 114, 163(1985)

3. P.I. Presunka and J.A. Coxon, J. Chem.Phys. 101, 201(1994)

4. P.I. Presunka and J.A. Coxon, Can.J.Chem. 71,1689(1993)

5. D.A. Fletcher, K.Y. Jung, C.T.Scurlock and T.C. Steimle, J. Chem.Phys. 98,1837 (1993)

6. M.A. Anderson, W.L. Barclay and L.M. Ziurys, Chem.Phys.Lett. 196,166 (1992)

7. D.A. Fletcher, M.A. Anderson, W.L. Barclay and L.M. Ziurys, J. Chem.Phys. 102, 4334 (1995)

8. T.C. Steimle, D.A. Fletcher, K.Y. Jun and C.T. Scurlock, J.Chem.Phys. 96, 2556 (1992)

9. J.M. Mestdagh and J.P. Visticot, Chem.Phys. 155,79 (1991)

10. A.R. Allouche and M. Aubert-Frecon, J.Mol.Spectrosc. 153, 599 (1994)

11. S. Gerstenkorn and P. Luc. Atlas du Spectre d'Absorption de la Molécule d'Iode. Laboratoire Aimé-Cotton,CNRS II - 91405 Orsay, France. 1978.

12. M. Douay, S. A. Rogers, and P.F. Bernath, Mol. Phys. 64, 425 (1988)

13. I. Kopp and J.T. Hougen, Can. J. Phys. 45, 2581 (1967)

14. R.N. Zare, A.L. Schmeltekopf, W.J. Harrop and D.L. Albritton, J. Mol. Spectrosc. 46, 37 (1973).

CHAPTER 4

HIGH RESOLUTION LASER EXCITATION SPECTROSCOPY OF THE $\tilde{B}^2B_1 - \tilde{X}^2A_1$ SYSTEM OF JET-COOLED $CaNH_2$

4.1 Introduction

Studies on the $CaNH_2$ radical date back to the early 1980s (1). Calcium vapor was mixed with hydrazine (N_2H_4) in a Broida oven and a weak chemiluminescence was observed which was attributed to $CaNH_2$ by comparison with the isoelectronic molecule CaF. Using high resolution laser spectroscopy, a partial rotational analysis of the $K_a = 1$ sub-band of the 0_0^0 band of the $\tilde{C}^2A_1 - \tilde{X}^2A_1$ transition was carried out (2). $CaNH_2$ was found to be a planar molecule with C_{2v} symmetry in both states. Subsequently, $CaNH_2$ and $SrNH_2$ were also produced in a Broida oven by exciting the $^3P_1$ - $^1S_0$ atomic transition of Ca or Sr in the presence of NH_3 (3). Low resolution spectra were recorded and the two broad features with maxima at 15 605 and 15 802 cm^{-1} were assigned to the $\tilde{A}^2B_2 - \tilde{X}^2A_1$ and $\tilde{B}^2B_1 - \tilde{X}^2A_1$ transitions of $CaNH_2$. A partial analysis of the $0_0^0\ \tilde{A}^2B_2 - \tilde{X}^2A_1$ and the $0_0^0\ \tilde{B}^2B_1 - \tilde{X}^2A_1$ band systems were performed by using the supersonic-jet expansion technique and a pulsed dye laser (4). Limited by the resolution of the dye laser, however, the accuracy of the derived molecular constants were not very high. The most recent study on $CaNH_2$ was carried out by using supersonic beam expansion combined with a high resolution cw ring dye laser system (5). The $\tilde{A}^2B_2 - \tilde{X}^2A_1$

band system was rotationally analyzed and the ground state dipole moment was determined from the Stark effect.

In this chapter, the high resolution analysis of the $\widetilde{B}^2B_1 - \widetilde{X}^2A_1$ and the $\widetilde{C}^2A_1 - \widetilde{X}^2A_1$ band systems will be discussed. The spectrum was recorded using the supersonic molecular beam spectrometer. The $K_a' = 1 - K_a'' = 0$, $K_a' = 0 - K_a'' = 1$ and $K_a' = 2 - K_a'' = 1$ sub-bands of the $\widetilde{B}^2B_1 - \widetilde{X}^2A_1$ transition and the $K_a' = 0 - K_a'' = 0$, $K_a' = 1 - K_a'' = 1$ sub-bands of the $\widetilde{C}^2A_1 - \widetilde{X}^2A_1$ transition were recorded and analyzed.

4.2 Experiment

The experimental apparatus has been discussed in previous chapters, so that only specific details about this experiment will be provided here. A pulse of 532 nm radiation from a Nd/YAG laser was focused onto a rotating calcium rod. Ammonia gas was used as the reactant and diluted (5%) in argon. After the pulsed valve was opened, the ammonia/argon was mixed with the Ca plasma during the supersonic expansion into vacuum.

A heavier carrier gas, argon, was used in order to get a lower rotational temperature, and the gas mixture travels more slowly than when helium is used. A time delay of 180 μs was needed for the molecules travel 120 mm from the nozzle to the probe region. Kiton red dye at about 620 nm was used in the Coherent 699-29 laser. In this experiment,

skimmer and the plate between the two chambers was taken out because it was found that the home made stainless steel skimmer disturbed the molecular beam. The spectrum of SrOD discussed in the previous chapter was hotter than expected because of the skimmer and it was very difficult to see any signal when argon was used as the carrier gas. With the skimmer and the plate removed a very good spectrum was recorded when argon was used.

With the help of previous work (6) three sub-bands: 0 - 1 ($K_a' = 0 - K_a'' = 1$), 1 - 0 ($K_a' = 1 - K_a'' = 0$) and 2 - 1 ($K_a' = 2 - K_a'' = 1$) of the $\tilde{B}^2B_1 - \tilde{X}^2A_1$ transition and the 0 - 0 ($K_a' = 0 - K_a'' = 0$) and 1 - 1 ($K_a' = 1 - K_a'' = 1$) sub-bands of the $\tilde{C}^2A_1 - \tilde{X}^2A_1$ transition were easily recorded. The laser excitation spectrum of I_2 was used to calibrate the absolute wavenumber scale.

4.3 Results and discussion

4.3.1 Electronic structure of $CaNH_2$

As discussed in chapter 3, the electronic energy structure of the calcium halides can be considered as that of a Ca^+ ion perturbed by the electric field of the negative halide ion. The ground state of the $CaNH_2$ molecule is essentially a 4s atomic orbital and the low-lying excited state orbitals result from a mixture of 3d and 4p Ca^+ atomic orbitals. For a linear molecule such as CaOH, there are five low-lying excited electronic states ($2 \times {}^2\Pi$, $2 \times {}^2\Sigma$, and ${}^2\Delta$) (Figure 4.1). In case of $CaNH_2$, which has C_{2v} symmetry, the ${}^2\Sigma$ states

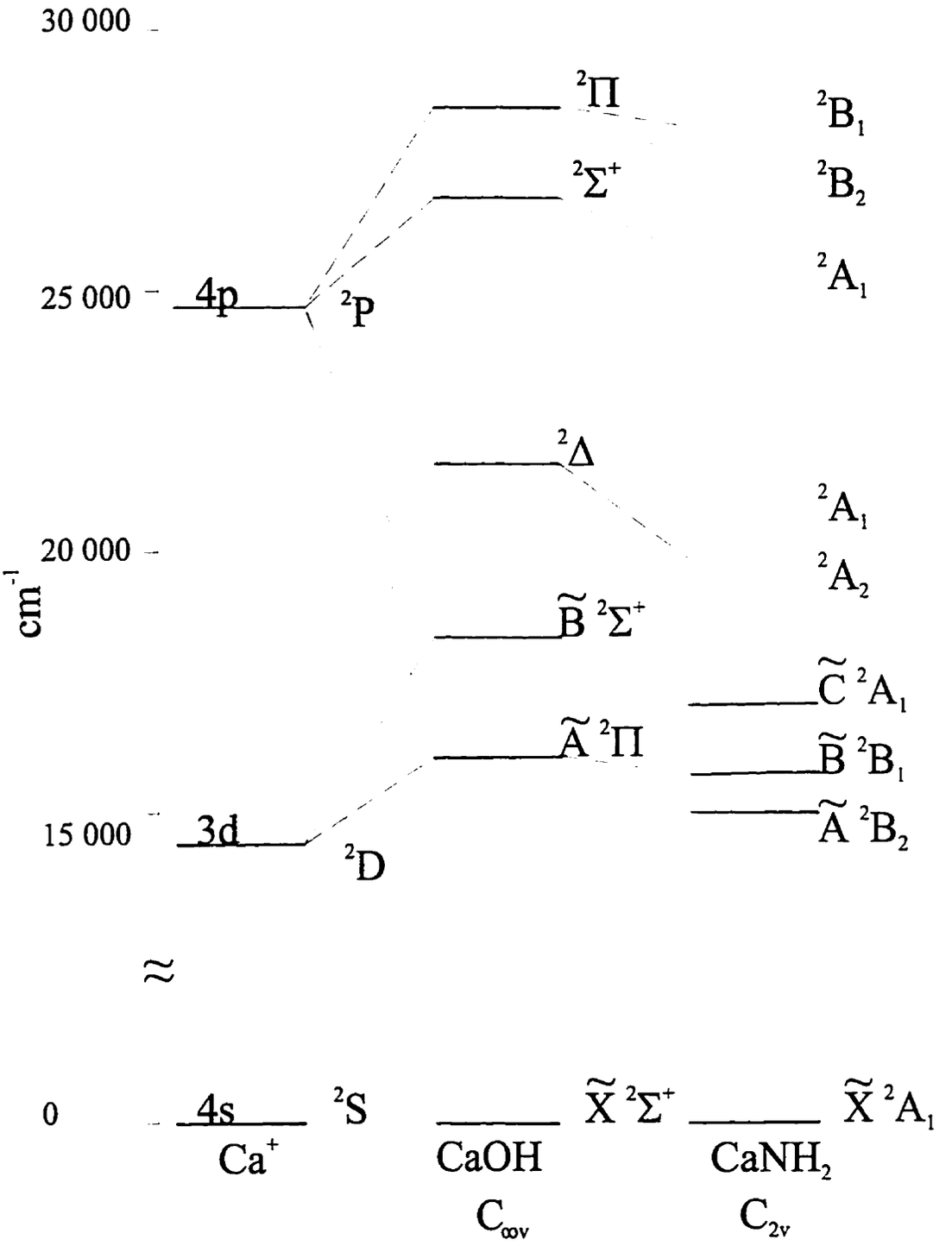

Figure 4.1 Correlation Diagram for $CaNH_2$

correlate to $^2A_1$ states, the orbitally degenerate $^2\Pi$ states are split into $^2B_1$ and $^2B_2$ states and $^2\Delta$ states split into $^2A_2$ and $^2A_1$ states.

4.3.2 Results for the $\tilde{B}^2B_1 - \tilde{X}^2A_1$ transition

$CaNH_2$ is an asymmetric top molecule with C_{2v} symmetry, and the $\tilde{B}$ state has B_1 symmetry, so that for the following integral to be nonzero

$$\int \psi_{el} \vec{\mu} \psi_{gs} dz$$

$\vec{\mu}$ must have b_1 symmetry, because ψ_{el} has a b_1 symmetry and ψ_{gs} has a a_1 symmetry. Thus the transition should be a c-type transition and the selection rules are:

$$\Delta K_a = \pm 1 \ (\pm 3, \pm 5, \ldots) \qquad (4.1)$$

$$\Delta K_c = 0 \ (\pm 2, \pm 4, \ldots) \qquad (4.2)$$

$$\Delta J = 0, \pm 1 \qquad (4.3)$$

The possible sub-band (K_a', K_a'') transitions are 0 - 1, 1 - 0, 2 - 1, 1 - 2, 3 - 2, 2 - 3, etc. Because of the cooling of the supersonic jet, however, only the low K_a value sub-bands 0 - 1, 1 - 0, and 2 - 1 were recorded since the nuclear spin statistics of the two hydrogen nuclei prevent $K_a'' = 1$ from cooling into $K_a'' = 0$.

Figure 4.2 is the spectrum for the 0 - 1 sub-band which looks very much like a $^2\Sigma$ - $^2\Pi$ transition of a linear molecule. The rotational energy levels are depicted in Figure 4.3 in which the standard N_{KaKc} notation (7) was used to label each energy level. For a $K_a = 0$ manifold state, each rotational level splits into two levels of the same total parity due to

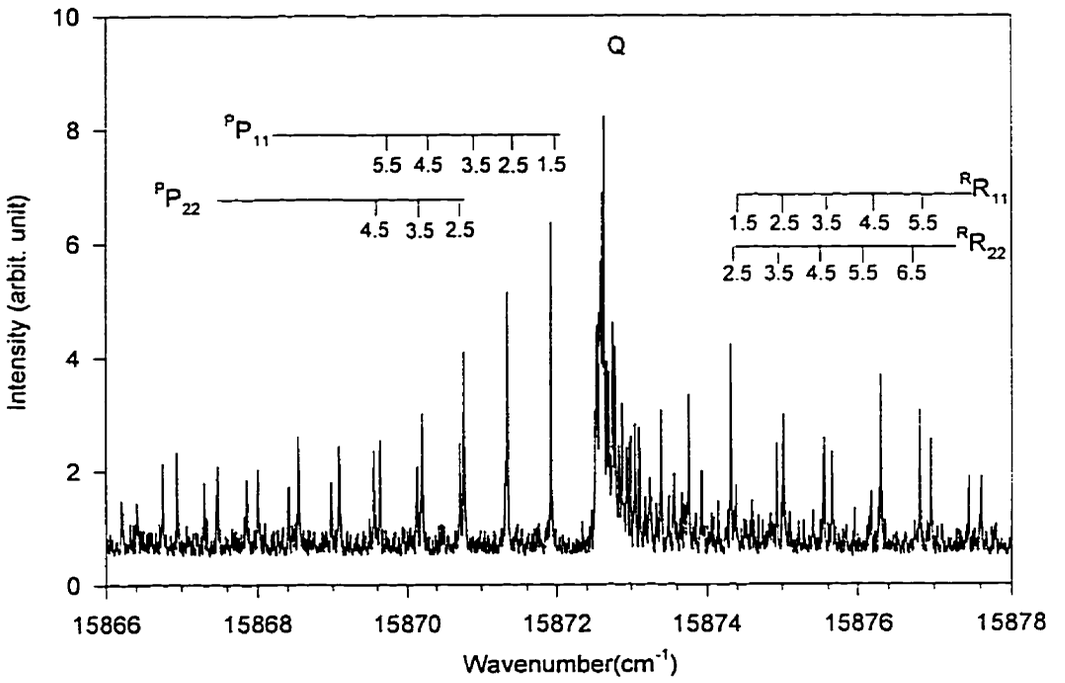

Figure 4.2 $K_a' = 0$ to $K_a'' = 1$ Sub-band of the $\widetilde{B}^2B_1$ - $\widetilde{X}^2A_1$ Transition

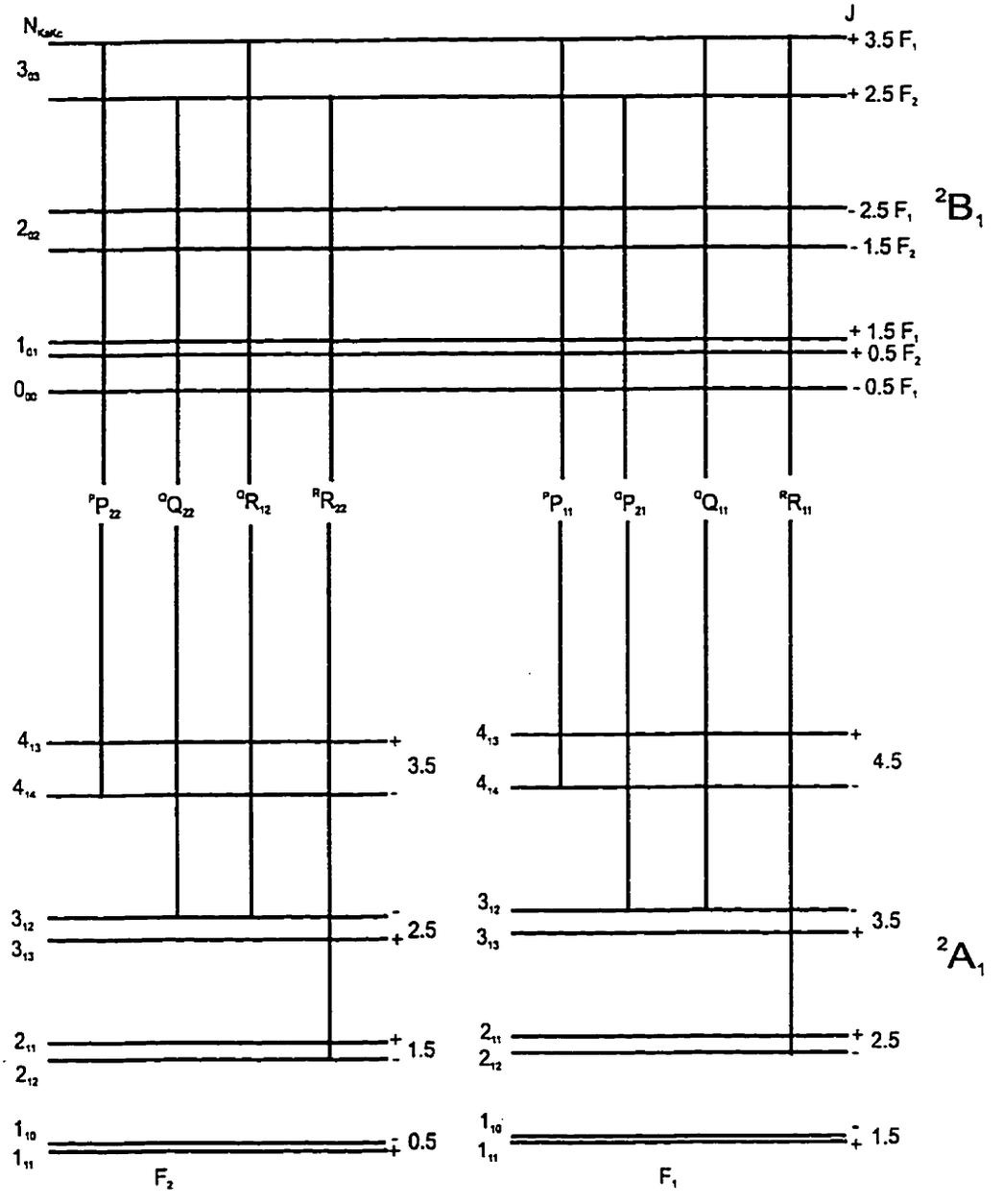

Figure 4.3 The Possible Transitions for the K_a = (0, 1) Sub-band of the $\widetilde{B}^2B_1$ - $\widetilde{X}^2A_1$ Transition

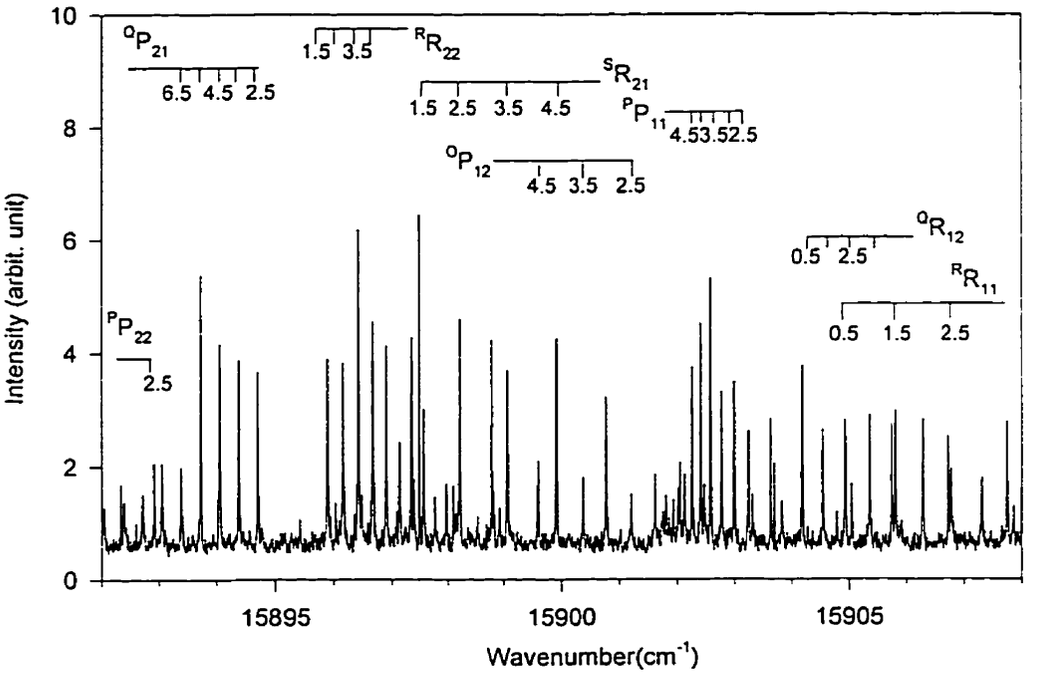

Figure 4.4 $K_a' = 1$ to $K_a'' = 0$ Sub-band of the $\tilde{B}^2B_1$ - $\tilde{X}^2A_1$ Transition

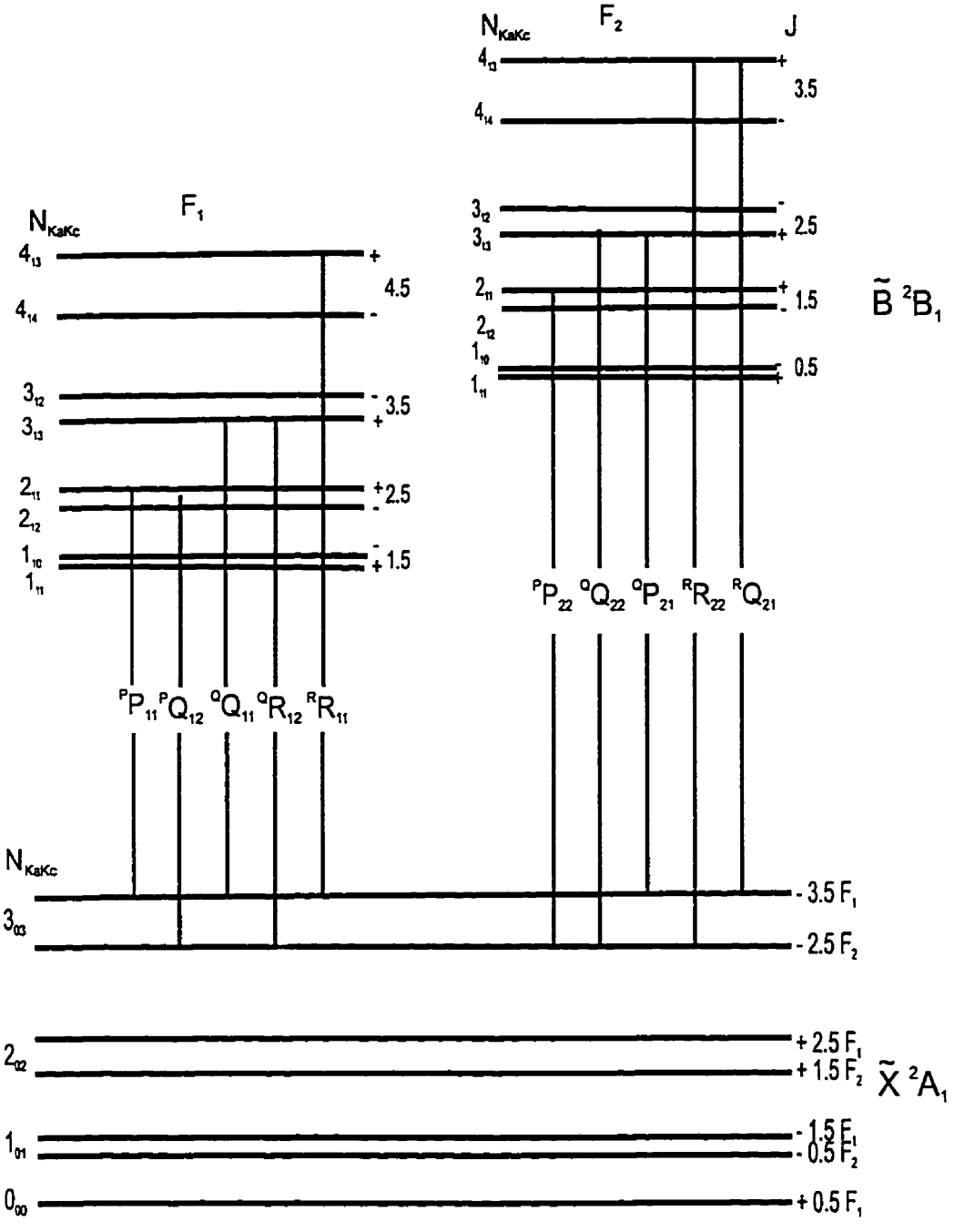

Figure 4.5 The Possible Transitions for the K_a = (1, 0) Sub-band of the $\widetilde{B}^2B_1$ - $\widetilde{X}^2A_1$ Transition

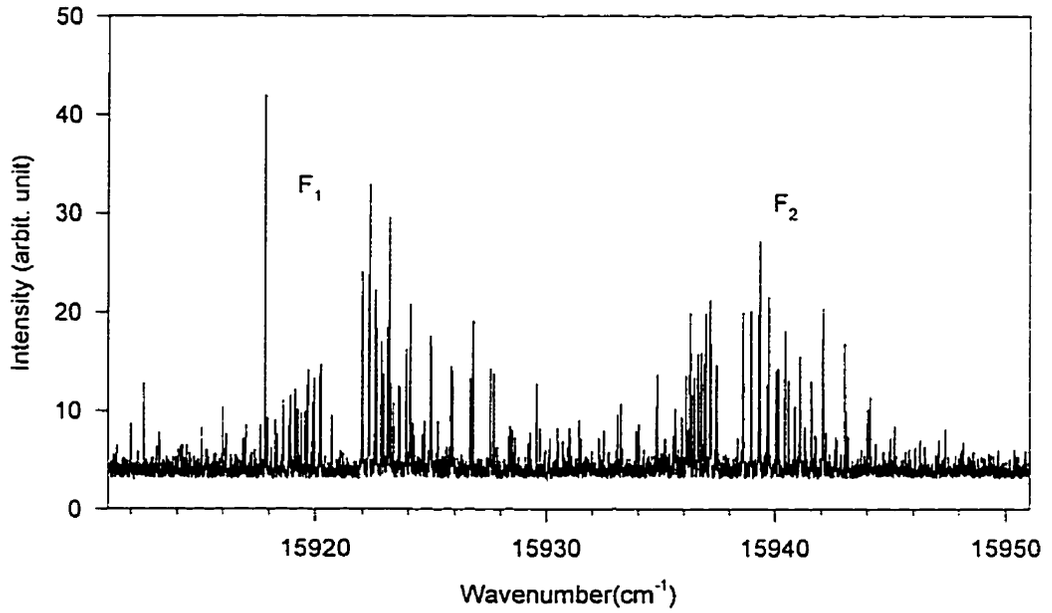

Figure 4.6 $K_a' = 2$ to $K_a'' = 1$ Sub-band of the $\widetilde{B}^2B_1$ - $\widetilde{X}^2A_1$ Transition

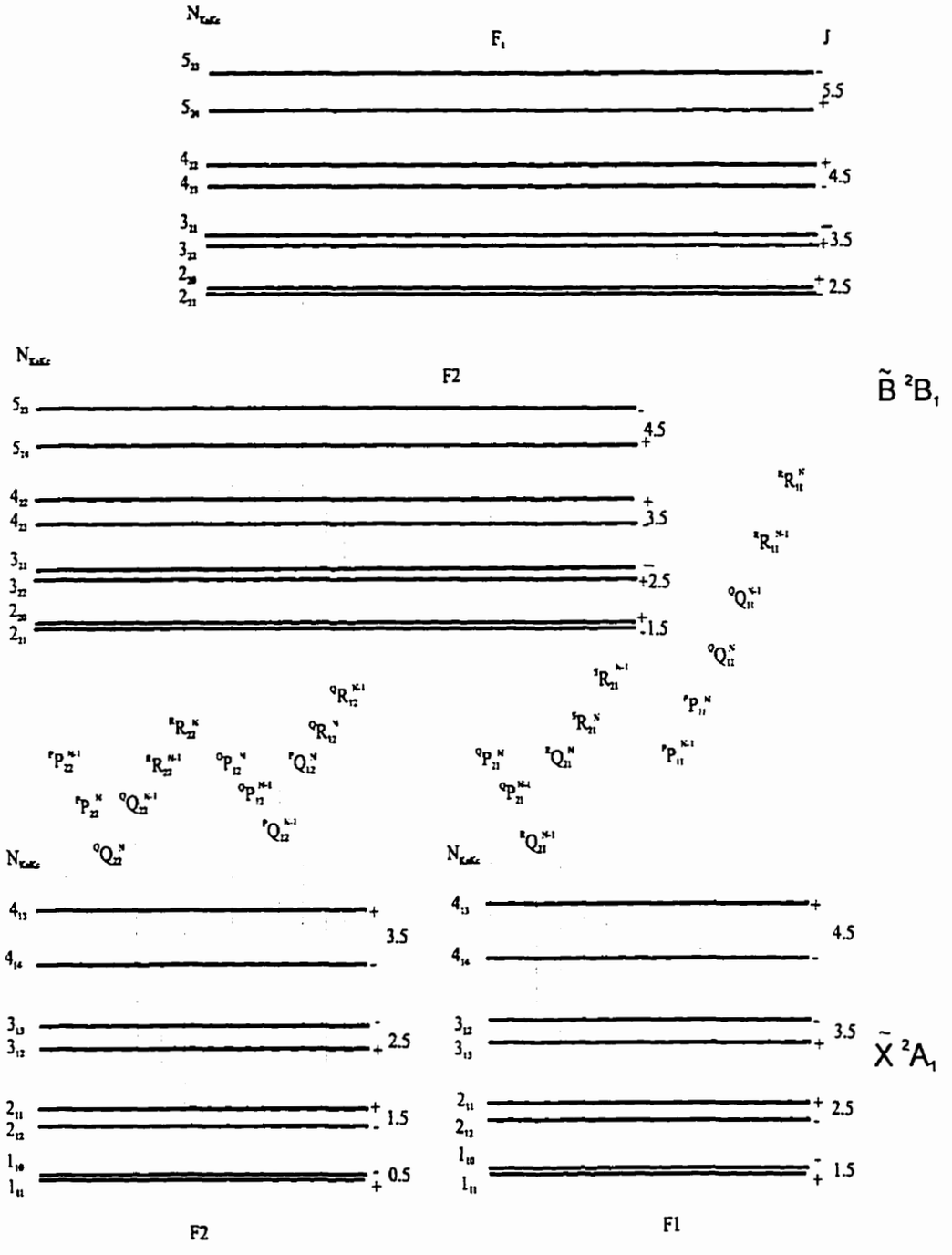

Figure 4.7 The Possible Transitions for the K_a = (2, 1) Sub-band of the $\tilde{B}^2B_1$ - $\tilde{X}^2A_1$ Transition

Table 4.1 Line for the K_a = (0 - 1) sub-band of $CaNH_2$

	J"	ν_{obs}	$\nu_{obs} - \nu_{cal}$		J"	ν_{obs}	$\nu_{obs} - \nu_{cal}$
$^{P}P_{11}$	1.5	15871.91995	-0.00401	$^{Q}Q_{22}$	1.5	15872.50962	0.0064
	2.5	15871.33622	-0.00695		2.5	15872.51863	0.00379
	3.5	15870.76415	-0.00451		3.5	15872.53408	-0.00454
	4.5	15870.19876	-0.00165		4.5	15872.55609	-0.00341
	5.5	15869.64338	0.00493		5.5	15872.58475	-0.00394
	6.5	15869.093	0.01015		6.5	15872.62016	-0.0069
	7.5	15868.54262	0.00892		7.5	15872.66239	0.00049
	8.5	15867.99724	0.00611		8.5	15872.71148	0.00462
	9.5	15867.46521	0.00994		9.5	15872.76746	0.00282
	10.5	15866.92817	0.00185		10.5	15872.83029	-0.00133
	11.5	15866.40114	-0.00334		11.5	15872.89985	-0.00526
	12.5	15865.89078	0.00085		12.5	15872.97591	0.00058
	13.5	15865.3821	-0.0008				
				$^{Q}Q_{11}$	1.5	15872.5379	0.00282
$^{R}R_{11}$	2.5	15874.37832	-0.00264		2.5	15872.56041	-0.00133
	3.5	15875.00542	-0.0077		3.5	15872.58922	-0.00526
	4.5	15875.6442	-0.00744		4.5	15872.62432	0.00058
	5.5	15876.29798	0.00138		5.5	15872.66578	0.00259
	6.5	15876.95177	0.00364		6.5	15872.71368	0.002
	7.5	15877.60722	0.00085		7.5	15872.76815	0.003
	8.5	15878.27268	0.00118		8.5	15872.82934	0.00499
	9.5	15878.94481	0.0011		9.5	15872.89743	0.00077
	10.5	15879.62195	-0.00127		10.5	15872.97261	-0.00245
	11.5	15880.31076	0.00055		11.5	15873.05508	-0.00543
	12.5	15881.00457	-0.00029		12.5	15873.14505	-0.00528
$^{P}P_{22}$	2.5	15870.71412	-0.00484				
	3.5	15870.13205	0.00119	$^{Q}Q_{12}$	1.5	15871.34521	0.00109
	4.5	15869.54831	-0.00092		2.5	15870.7718	0.01023
	5.5	15868.97125	-0.00292		3.5	15870.20459	-0.00129
	6.5	15868.40586	0.001		4.5	15869.64365	0.00182
	7.5	15867.8488	0.00467		5.5	15869.08906	-0.00073
	8.5	15867.29008	0.00077		6.5	15868.54091	-0.00139
	9.5	15866.74304	0.00167		7.5	15867.99932	-0.00067
	10.5	15866.19599	-0.00433		8.5	15867.46445	0.0044
	11.5	15865.66396	-0.00217		9.5	15866.93649	0.00317
$^{R}R_{22}$	1.5	15874.30494	-0.00433	$^{Q}Q_{21}$	1.5	15873.7023	-0.00922
	2.5	15874.92036	-0.00147		2.5	15874.30724	-0.01852
	3.5	15875.54079	-0.00014		3.5	15874.91871	0.0027
	4.5	15876.16956	0.00289		4.5	15875.53676	0.00057
	5.5	15876.80333	0.00419		5.5	15876.16147	0.00092
	6.5	15877.44044	0.00202		6.5	15876.79294	0.00557
	7.5	15878.08755	0.00299		7.5	15877.43122	0.00201
	8.5	15878.74134	0.00375		8.5	15878.07637	-0.00063

Table 4.2 Lines for the K_a = (1 - 0) sub-band $CaNH_2$

	J"	ν_{obs}	$\nu_{obs} - \nu_{cal}$		J"	ν_{obs}	$\nu_{obs} - \nu_{cal}$
$^{Q}P_{21}$	2.5	15894.69198	-0.002	$^{R}R_{22}$	0.5	15895.87946	-0.00139
	3.5	15894.37509	0.00095		1.5	15896.14965	-0.00067
	4.5	15894.0482	0.00021		2.5	15896.41317	0.0044
	5.5	15893.7213	0.00387		3.5	15896.66	0.00317
	6.5	15893.38441	0.00259		4.5	15896.89683	0.00137
	7.5	15893.05084	-0.0002		5.5	15897.12366	-0.00213
	8.5	15892.71728	-0.00183		6.5	15897.34381	-0.00525
	9.5	15892.39038	0.00259		7.5	15897.55729	-0.00922
	10.5	15892.04348	-0.02325		8.5	15897.76077	-0.01853
	11.5	15891.72993	-0.01937				
				$^{Q}Q_{22}$	1.5	15894.69643	-0.002
$^{S}R_{21}$	1.5	15897.34381	0.00223		2.5	15894.37756	0.00095
	2.5	15898.20441	0.00242		3.5	15894.05239	0.00021
	3.5	15899.05833	0.00037		4.5	15893.72281	0.00387
	4.5	15899.91225	0.00076		5.5	15893.3908	-0.002
	5.5	15900.76618	0.00164		6.5	15893.05836	-0.0002
	6.5	15901.61677	-0.00227		7.5	15892.72742	-0.00183
	7.5	15902.46736	-0.00941		8.5	15892.39975	-0.002
	8.5	15903.31794	-0.02141		9.5	15892.07699	-0.02325
					10.5	15891.76053	-0.01937
$^{O}P_{12}$	2.5	15901.19648	0.00872		11.5	15891.45153	0.00259
	3.5	15900.37591	0.00557		12.5	15891.15081	-0.07272
	4.5	15899.58536	0.00201				
	5.5	15898.82484	-0.00063	$^{Q}Q_{11}$	1.5	15904.15177	0.00259
	6.5	15898.09099	-0.00387		2.5	15904.51993	0.00499
	7.5	15897.3805	-0.00879		3.5	15904.91851	0.00077
					4.5	15905.34615	-0.00245
$^{Q}R_{12}$	0.5	15904.17187	0.01863		5.5	15905.80104	-0.00543
	1.5	15904.52878	0.0064		6.5	15906.28091	-0.00528
	2.5	15904.92572	0.00379		7.5	15906.78324	0.00109
	3.5	15905.34601	-0.00454		8.5	15907.30524	0.01023
	4.5	15905.803	-0.00341		9.5	15907.84399	0.00259
	5.5	15906.28333	-0.00394		10.5	15908.39648	-0.00129
	6.5	15906.78367	-0.0069		11.5	15908.95959	0.00183
	7.5	15907.31404	0.00049		12.5	15909.53017	-0.00073

Table 4.2 Lines for the K_a = (1 - 0) sub-band $CaNH_2$ (continued)

	J''	ν_{obs}	$\nu_{obs} - \nu_{cal}$		J''	ν_{obs}	$\nu_{obs} - \nu_{cal}$
$^{P}P_{11}$	2.5	15902.99105	0.00462	$^{P}Q_{12}$	1.5	15902.96714	-0.00067
	3.5	15902.7709	0.00283		2.5	15902.74299	0.0044
	4.5	15902.5741	-0.00133		3.5	15902.54927	0.00317
	5.5	15902.40064	-0.00526		4.5	15902.38463	0.00137
	6.5	15902.25721	0.00058		5.5	15902.24725	-0.00213
	7.5	15902.12712	0.00259		6.5	15902.13488	-0.00525
	8.5	15901.93365	-0.07272		7.5	15902.04498	-0.00922
	9.5	15901.75019	-0.14865		8.5	15901.97478	0.00095
					9.5	15901.92137	0.00021
$^{R}R_{11}$	0.5	15904.77228	0.00499		10.5	15901.88172	0.00387
	1.5	15905.73628	0.00077				
	2.5	15906.72697	-0.00245	$^{R}Q_{21}$	1.5	15895.88106	0.00259
	3.5	15907.741	-0.00543		2.5	15896.1545	-0.02325
	4.5	15908.77839	-0.00528		3.5	15896.42163	-0.01937
	5.5	15909.83912	0.00109		4.5	15896.68433	0.00259
	6.5	15910.91653	0.01023		5.5	15896.94459	-0.003
					6.5	15897.2044	0.002
$^{P}P_{22}$	2.5	15892.91408	-0.00129		7.5	15897.46567	0.0003
	3.5	15892.00011	0.00183		8.5	15897.73021	0.00499
	4.5	15891.06947	-0.00073		9.5	15897.99961	0.00077

Table 4.3 Lines for the K_a = (2 - 1) sub-band F_2 of $CaNH_2$

	J''	ν_{obs}		J''	ν_{obs}
$^{O}P_{21}^{N-1}$	2.5	15937.40245	$^{P}P_{22}^{N-1}$	3.5	15934.75729
	3.5	15937.14561		4.5	15933.92004
	4.5	15936.90211		5.5	15933.09614
	5.5	15936.67195		6.5	15932.29003
	6.5	15936.46847			
	7.5	15936.27501	$^{R}R_{22}^{N-1}$	1.5	15938.93685
	8.5	15936.09488		2.5	15939.29154
	9.5	15935.92143		3.5	15939.66402
	10.5	15935.64568		4.5	15940.04539
				5.5	15940.45456
$^{S}R_{21}^{N-1}$	1.5	15940.13101		6.5	15940.87152
	2.5	15941.085		7.5	15941.30515
	3.5	15942.049		8.5	15941.75102
	4.5	15943.03301		9.5	15942.21912
	5.5	15944.03371		10.5	15942.695
	6.5	15945.04441		11.5	15943.18979
	7.5	15946.07512			
	8.5	15947.11917	$^{P}P_{22}^{N}$	3.5	15934.83623
				4.5	15934.03234
$^{O}P_{21}^{N}$	2.5	15937.42691		5.5	15933.25069
	3.5	15937.19008		6.5	15932.49572
	4.5	15936.97771			
	5.5	15936.78536	$^{R}R_{22}^{N}$	1.5	15938.96131
	6.5	15936.62858		2.5	15939.33935
	7.5	15936.47514		3.5	15939.7374
	8.5	15936.36173		4.5	15940.1588
				5.5	15940.61245
$^{S}R_{21}^{N}$	1.5	15940.14101		6.5	15941.1039
	2.5	15941.10501		7.5	15941.56978
	3.5	15942.0957			
	4.5	15943.1064			
	5.5	15944.14712			
	6.5	15945.20563			
	7.5	15946.2886			
	8.5	15947.39381			

Table 4.3 (2 - 1) subband F1

	J"	ν_{obs}	$\nu_{obs} - \nu_{cal}$		J"	ν_{obs}	$\nu_{obs} - \nu_{cal}$
$^{P}P_{11}^{N}$	3.5	15920.24319	0.00239	$^{Q}Q_{11}^{N}$	2.5	15922.00601	-0.00385
	4.5	15919.95966	0.00042		3.5	15922.31147	-0.00634
	5.5	15919.6828	0.00094		4.5	15922.63751	0.00758
	6.5	15919.40928	0.0005		5.5	15922.95297	0.00663
	7.5	15919.13909	-0.00099		6.5	15923.27004	0.00291
	8.5	15918.87891	0.00314		7.5	15923.59448	0.00216
	9.5	15918.61651	0.00073		8.5	15923.92481	0.003
	10.5	15918.36522	0.00535		9.5	15924.25111	-0.00427
					10.5	15924.58809	-0.00449
$^{R}R_{11}^{N}$	1.5	15923.18781	-0.00165		11.5	15924.92451	-0.00821
	2.5	15924.0851	-0.00178		12.5	15925.27958	0.00479
	3.5	15924.98683	-0.00166		13.5	15925.62399	0.00665
	4.5	15925.89635	0.00195		14.5	15925.96191	0.00351
	5.5	15926.80142	-0.00327				
	6.5	15927.71427	-0.00511	$^{Q}Q_{11}^{N-1}$	2.5	15921.99108	0.00387
	7.5	15928.63491	-0.00345		3.5	15922.27322	0.00075
	8.5	15929.56222	0.00081		4.5	15922.5529	-0.00143
	9.5	15930.47952	-0.00856		5.5	15922.83195	-0.00091
					6.5	15923.10617	-0.00191
$^{P}P_{11}^{N-1}$	3.5	15920.19983	0.00435		7.5	15923.38369	0.00375
	4.5	15919.88294	-0.00076		8.5	15923.64981	0.00157
	5.5	15919.56939	0.00088		9.5	15923.91012	-0.00248
	6.5	15919.25139	0.00141		10.5	15924.17439	0.00201
	7.5	15918.93228	0.00412		11.5	15924.42437	-0.00227
	8.5	15918.6065	0.00352		12.5	15924.67098	-0.00305
	9.5	15918.28294	0.00869		13.5	15924.91588	0.00322
					14.5	15925.13836	-0.0016
$^{R}R_{11}^{N-1}$	2.5	15924.06286	-0.00134				
	3.5	15924.94236	-0.00074				
	4.5	15925.81741	-0.00127				
	5.5	15926.68801	-0.00295				
	6.5	15927.5575	-0.00236				
	7.5	15928.42588	0.00067				
	8.5	15929.28425	-0.00235				
	9.5	15930.14596	0.00255				
	10.5	15931.01322	0.01853				

spin-rotation interaction. They are labeled as F_1 or F_2 according to whether J = N + 1/2 or J = N - 1/2. For a $K_a \neq 0$ state, the spin-rotation interaction splits each rotational level into F_1 and F_2 components and then each level splits into a closely spaced asymmetry doublet. This pattern of energy levels results in 12 branches for the 0 - 1 sub-band. The notation for each branch, ${}^{\Delta N}\Delta J F_i' F_i''$, follows the recommendations in Reference (5). Because some of the splittings are very small, not all of the possible branches are resolved. The measured and assigned line positions are listed in Table 4.1.

Figure 4.4 shows the spectrum for the 1 - 0 sub-band. This sub-band is similar to 0 - 1 sub-band and looks like a ${}^2\Pi$ - ${}^2\Sigma$ transition with 12 possible branches. The energy level pattern is depicted in Figure 4.5. The line positions are listed in Table 4.2.

The spectrum for the 2 - 1 sub-band is illustrated in Figure 4.6 and the energy level diagram is provided in Figure 4.7. In this case there is both spin-rotation and asymmetry splitting for the upper and lower energy states, and 24 branches are possible. They are designated using the same notation as for 0 - 1 sub-band but a right superscript, N″ or N″-1, is used to indicate the K_c' value. Only the resolved branches are listed in Table 4.3.

4.3.3 Results for the $\tilde{C}^2A_1 - \tilde{X}^2A_1$ transition

$CaNH_2$ is an asymmetric top molecule with C_{2v} symmetry, and the $\tilde{C}$ state has A_1 symmetry, so that for the following integral to be nonzero

$$\int \psi_{el} \vec{\mu} \psi_{gs} dz$$

$\vec{\mu}$ must have a_1 symmetry, because ψ_{el} has b_1 symmetry and ψ_{gs} has a_1 symmetry. The transition should be an a-type parallel transition and the selection rules are:

$$\Delta K_a = \pm 0(\pm 2, \pm 4, \ldots) \qquad (4.1)$$

$$\Delta K_c = \pm 1\ (\pm 3, \pm 5, \ldots) \qquad (4.2)$$

$$\Delta J = 0,\ \pm 1 \qquad (4.3)$$

Therefore the possible sub-bands (K_a', K_a'') transitions are 0 - 0, 1 - 1, 2 - 2, ..., however, because of the cooling of the supersonic jet, only 0 - 0 and 1 - 1 sub-bands were recorded. The detailed analysis of this transition was carried out by Zulfikar Morbi (11) .

4.3.4 Analysis

Only transitions with small J values were recorded so the effect of centrifugal distortions should be small, and the proton magnetic hyperfine interactions were not resolved. For the effective Hamiltonian operator only the rotational and spin-rotational interactions (8) need to be considered,

$$\hat{H}_{eff} = \hat{H}_{rot} + \hat{H}_{sr} \qquad (4.1)$$

where H_{rot} is the rotational Hamiltonian for an asymmetric rotor, including the effects of centrifugal distortion to the fourth power (9),

$$\hat{H}_{rot} = A\hat{J}_a^2 + \tfrac{1}{2}(B+C)(\hat{J}^2 - \hat{J}_a^2) - D_k\hat{J}_a^4 - D_{JK}\hat{J}^2(\hat{J}^2 - \hat{J}_a^2)$$

$$-D_J\hat{J}^4+\tfrac{1}{2}(B-C)(\hat{J}_b^2-\hat{J}_c^2)-2\delta_J\hat{J}^2(\hat{J}_b^2-\hat{J}_c^2)$$
$$-\delta_K(\hat{J}_a^2(\hat{J}_b^2-\hat{J}_c^2)+(\hat{J}_b^2-\hat{J}_c^2)\hat{J}_a^2) \qquad (4.2)$$

which has the matrix elements given in Table 4.4,

Table 4.4 Matrix elements for the non-rigid asymmetric rotor

$\langle J,K\vert\hat{H}_{rot}\vert J,K\rangle = AK^2+\tfrac{1}{2}(B+C)[J(J+1)-K^2]$ $-D_K K^4-D_{JK}J(J+1)K^2-D_J J^2(J+1)^2$
$\langle J,K\vert\hat{H}_{rot}\vert J,K\pm2\rangle=[\tfrac{1}{4}(B-C)-\delta_J J(J+1)-\tfrac{1}{2}\delta_K(K^2+(K\pm2)^2)]$ $\times[J(J+1)-K(K\pm1)]^{\frac{1}{2}}[J(J+1)-(K\pm1)(K\pm2)]^{\frac{1}{2}}$

In the coupled Hund's case (b) basis, $|NJSK\rangle$, the spin-rotation interaction H_{sr} is represented in the A-reduced form as

$$\begin{aligned}
\hat{H}_{sr} &= \hat{H}_{sr}^{(2)} + \hat{H}_{sr}^{(4)} \\
\hat{H}_{sr}^{(2)} &= \varepsilon_{aa} N_a S_a + \varepsilon_{bb} N_b S_b + \varepsilon_{cc} N_c S_c + \tfrac{1}{2}(\varepsilon_{ab} + \varepsilon_{ba}) \times (N_b S_a + N_a S_b) \\
\hat{H}_{sr}^{(4)} &= \Delta_N^S N^2 (N \bullet S) + \tfrac{1}{2}\Delta_{NK}^S (N^2 N_z S_z + N_z S_z N^2) \\
&\quad + \Delta_{NK}^S N_z^2 (N \bullet S) + \Delta_K^S N_z^3 S_z + \delta_N^s (N_+^2 + N_-^2) \\
&\quad \times (N \bullet S) + \tfrac{1}{2}\delta_K^S [(N_+^2 + N_-^2) N_z S_z + N_z S_z (N_+^2 + N_-^2)]
\end{aligned} \tag{4.3}$$

and the matrix elements are listed in Table 4.5 (9). The matrix elements of Table 4.5 must be added to those of Table 4.4, with J replaced by N to form the complete spin-molecular rotation matrix. The $\hat{H}_{rot}$ term gives rise to matrix elements of the form $\Delta N = 0$, $\Delta K = 0$, ± 2 and $\Delta J = 0$, whereas the $\hat{H}_{sr}$ terms gives rise to $\Delta J = 0$, $\Delta K = 0, \pm 1, \pm 2$ type matrix elements.

The matrix elements of all necessary J's and K's can be calculated using the matrix elements of Table 4.4 and 4.5. Diagonalizing the Hamiltonian matrix then gives the eigenvalues and eigenvectors. Fortunately a computer program was already written to fit the data (10). A standard nonlinear least-squares fitting procedure was used to fit the observed line positions to obtain the molecular parameters. In the final fit the $\tilde{X}^2 A_1$ rotational and spin-rotational parameters were fixed to the previously determined values (5). The fitted spectroscopic parameters are given in Table 4.6.

Table 4.5 Matrix elements of the spin-rotation Hamiltonian and its centrifugal distortion for an asymmetric top molecule in a doublet electronic state

$$\langle NKSJ|H_{sr}|NKSJ\rangle = -[G(NSJ)/2N(N+1)]\{\varepsilon_{aa}+(\varepsilon_{bb}+\varepsilon_{cc})$$
$$\times[N(N+1)-K^2]/2+\Delta^s_K K^4+(\Delta^s_{NK}+\Delta^s_{KN})K^2N(N+1)+\Delta^s_N N^2(N+1)^2\}$$

$$\langle NK\pm1,SJ|H_{sr}|NKSJ\rangle = -[\Gamma(NSJ)(2K\pm1)/4N(N+1)]$$
$$\times[N(N+1)-K(K\pm1)]^{\frac{1}{2}}(\varepsilon_{ab}+\varepsilon_{ba})/2$$

$$\langle NK\pm2,SJ|H_{sr}|NKSJ\rangle = -[\Gamma(NSJ)/4N(N+1)][N(N+1)-K(K\pm1)]$$
$$\times[N(N+1)-(K\pm1)(K\pm2)]^{\frac{1}{2}}\{\varepsilon_{bb}-\varepsilon_{cc})/2+2\delta^s_N N(N+1)+\delta^s_K[K^2+(K\pm2)^2]\}$$

$$\langle N-1,KSJ|H_{sr}|NKSJ\rangle = -\Phi(NSJ)(K/2N)(N^2-K^2)^{\frac{1}{2}}$$
$$\times\{\varepsilon_{aa}-(\varepsilon_{bb}+\varepsilon_{cc})/2+\Delta^s_K K^2+\Delta^s_{NK}N^2\}$$

$$\langle N-1,K\pm1,SJ|H_{sr}|NKSJ\rangle = -\Phi(NSJ)[(N\pm2K+1)/4N]$$
$$\times[(N\mp K)(N\mp K-1)]^{\frac{1}{2}}(\varepsilon_{ab}+\varepsilon_{ba})/2$$

$$\langle N-1,K\pm2,SJ|H_{sr}|NKSJ\rangle = -[\Phi(NSJ)/4N][(N\mp K)(N\mp K-1)(N\mp K-2)$$
$$\times(N\pm K+1)]^{\frac{1}{2}}\{\pm(\varepsilon_{bb}-\varepsilon_{cc})/2+\delta^s_K[K(N\pm K)+(K\pm2)(N\pm K+2)]\}$$

$$\Gamma(NSJ) = N(N+1)+S(S+1)-J(J+1)$$

$$\Phi(NSJ) = [(N-J+S)(N+J+S+1)\times(S+J-N+1)(N+J-S)/2N+1)(2N-1)]^{\frac{1}{2}}$$

4.3.5 Discussion

As discussed in the previous section, the $\widetilde{A}^2B_2$ and the $\widetilde{B}^2B_1$ electronic states of $CaNH_2$ correlate with the $\widetilde{A}^2\Pi$ state and the $\widetilde{C}^2A_1$ state correlates with the $\widetilde{B}^2\Sigma^+$ state of the linear CaOH molecule (Figure 4.1). All three of these states arises mainly from an atomic ^2P state of Ca^+. In the "pure precession" limit, the $\widetilde{C}^2A_1$ state arises from a single unpaired electron in the 4pσ orbital of Ca^+ aligned along the Ca-N bond, and the $\widetilde{A}^2B_2$ and the $\widetilde{B}^2B_1$ states can be considered to have the unpaired electron in Ca^+ 4p orbitals in and out of the molecular plane but perpendicular to the Ca-N bond, respectively (Figure 4.8).

If there is no rotation of the molecule, there is no interaction between the $\widetilde{A}$, $\widetilde{B}$ and $\widetilde{C}$ states. In the rotating molecule, however, these electronic states interact by a mechanism analogous to Coriolis coupling between vibrational levels in a single electronic state. Rotation about the a-axis of the molecule couples the $\widetilde{A}^2B_2$ and the $\widetilde{B}^2B_1$ states, rotation about b-axis causes interaction between the $\widetilde{C}^2A_1$ and $\widetilde{B}^2B_1$ states and rotation about c-axis causes interaction between $\widetilde{C}^2A_1$ and $\widetilde{A}^2B_2$ states. The interactions caused by rotation will be discussed in the following sections.

Table 4.6. Fitted spectroscopic constants for the low-lying electronic state of $CaNH_2$ (cm^{-1})

	$\tilde{X}^2A_1$	$\tilde{A}^2B_1$	$\tilde{B}^2B_2$	$\tilde{C}^2A_1$
T_{00}	0	15464.36741(47)	15885.28204(11)	17375.16686(65)
A	13.05740(54)	11.44853(14)	14.41899(14)	12.95127(86)
B	0.300446(17)	0.307026(42)	0.30167(32)	0.305051(25)
C	0.292849(17)	0.299178(42)	0.29164(32)	0.297964(25)
ε_{aa}	0	8.2370(11)	-7.6194(20)	0.9985(11)
ε_{bb}	$9.77(73)\times10^{-4}$	$5.97(29)\times10^{-3}$	$-3.673(96)\times10^{-2}$	$-3.966(27)\times10^{-2}$
ε_{cc}	$9.77(73)\times10^{-4}$	$5.526(29)\times10^{-2}$	$7.914(96)\times10^{-2}$	$-3.084(27)\times10^{-2}$
Δ_K			$-2.050(38)\times10^{-2}$	
Δ_N			$-5.99(31)\times10^{-6}$	$1.0869(25)\times10^{-6}$
Δ_N			$1.71(89)\times10^{-3}$	$2.53(20)\times10^{-3}$
δ_K			$6.90(13)\times10^{-3}$	

A. a-axis rotation-electronic interaction

The rotation about the a-axis is actually the rotation of two protons, and the interaction between this rotation and the orbital angular momentum of the atomic ^{2}P state is the reason the electronic states couple together.

When the NH_2 group is not rotating, the $\tilde{A}$ and $\tilde{B}$ states will not interact and the orbital angular momentum of the ^{2}P state is quenched in a molecule. As the NH_2 group starts to rotate, at first the pπ electron will follow the motion adiabatically. As the hydrogens rotate faster and faster, the motion of the electron can not match the rotation of the NH_2 group and will decouple from the nuclear frame. In this case, the $\tilde{A}$ and $\tilde{B}$ states will mix and a net electronic orbital angular momentum will be induced in each state.

By analogy with the a-axis Coriolis and spin-orbit interaction Hamiltonian used in the "bent molecule" formalism for the Renner-Teller interaction of a triatomic molecule in a $^2\Pi$ state near the linear configuration, the following formula can be considered as a reasonable approximation of the interaction (6)

$$H_{int} = -2AN_aL_a + A^{so}L_aS_a \qquad (4.4)$$

where A is the "true" value of the a-axis rotation constant, A^{so} is the spin-orbit constant for the unperturbed parent $^2\Pi$ state. By replacing the angular momentum operators N_a, L_a

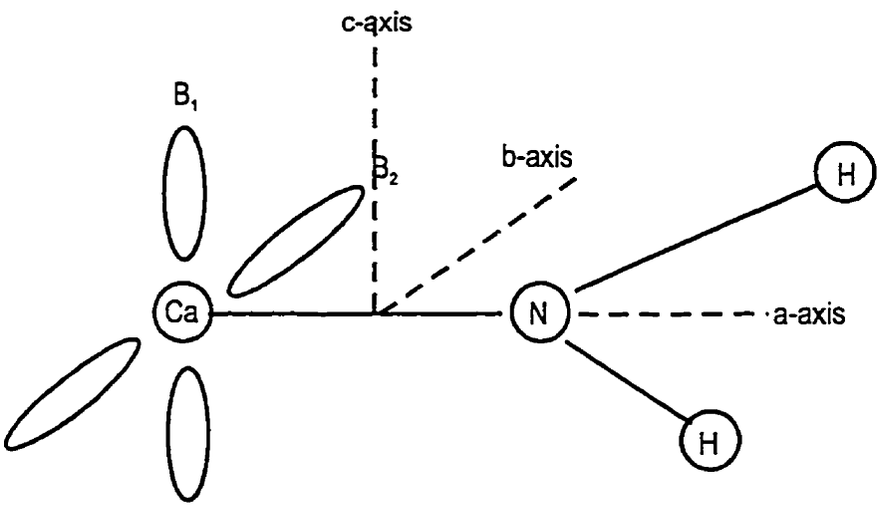

Figure 4.8 Orbital Structure of $CaNH_2$

and S_a by the corresponding quantum numbers, K_a, Λ and Σ, and letting E_a and E_b be the $\tilde{A}$ and $\tilde{B}$ state energies, respectively, a 2x2 matrix for the Hamiltonian can be formed

$$\begin{pmatrix} E_a - A(K_a^2+\Lambda^2) - E & -2AK_a\Lambda + A^{so}\Lambda\Sigma \\ -2AK_a\Lambda + A^{so}\Lambda\Sigma & E_a + A(K_a^2+\Lambda^2) - E \end{pmatrix} = 0 \quad (4.5)$$

Diagonalization of this matrix gives the perturbed energy levels. For the $\tilde{A}$ state (to second order)

$$E_a' = E_a + A(K_a^2+\Lambda^2) - \frac{A^{so}\Lambda^2\Sigma^2}{\Delta E} - \frac{4A^2\Lambda^2K_a^2}{\Delta E} + \frac{4AA^{so}\Lambda^2\Sigma K_a}{\Delta E} + \ldots, \quad (4.6a)$$

where $\Delta E = (E_b - E_a)$ and for the $\tilde{B}$ state,

$$E_a' = E_a + A(K_a^2+\Lambda^2) + \frac{A^{so}\Lambda^2\Sigma^2}{\Delta E} + \frac{4A^2\Lambda^2K_a^2}{\Delta E} - \frac{4AA^{so}\Lambda^2\Sigma K_a}{\Delta E} + \ldots \quad (4.6b)$$

The effect of this interaction on the A and ε_{aa} spectroscopic constants was derived for the $\tilde{A}$ and $\tilde{B}$ states in the pure precession limit as

$$A^{spec} = A \mp \frac{4\Lambda^2A^2}{\Delta E_{\tilde{B}-\tilde{A}}}, \qquad \varepsilon_{aa} = \pm\frac{4\Lambda^2AA^{so}}{\Delta E_{\tilde{B}-\tilde{A}}} \quad (4.7)$$

where, Λ is the component of the orbital angular momentum on the a-axis and $\Delta E_{\tilde{B}-\tilde{A}}$ is the energy difference $E(\tilde{B}) - E(\tilde{A})$. In these formulas, the top sign refers to the $\tilde{A}$ state and the lower to the $\tilde{B}$ state. Λ should be the same for both states, therefore

$$A = [A^{spec}(\tilde{A}) + A^{spec}(\tilde{B})]/2 \quad (4.8)$$

and from the spectroscopic constants in Table 4.8, we have

$$A = 12.93 \text{ cm}^{-1}$$

$$\Delta E = 420.91 \text{ cm}^{-1}$$

By substituting these values into formulas (4.7), we have

$$\Lambda \sim 1$$

$$A^{so} = 67.03 \text{ cm}^{-1}$$

For a pure $^2\Pi$ parent, the value for Λ should be unity and the above prediction gives a value very close to 1. The value for the spin-orbit constant A^{so} = 67.03 cm^{-1} is consistent with the measured values of 71 and 67 cm^{-1} for CaF and CaOH, respectively. These results indicate that the "pure precession" approximation can be used to explain the a-axis rotation electronic interaction almost perfectly.

B. End-over-end rotation-electronic interaction

In a similar fashion as in the case of the a-axis rotation, interactions between $\tilde{C}$ and $\tilde{B}$ states, and the interactions between $\tilde{C}$ and $\tilde{A}$ states were derived in the pure precession limit (11):

$$\varepsilon_{bb} = \pm \frac{2l(l+1)BA^{so}}{\Delta E_{\tilde{C}-\tilde{B}}}$$

$$\varepsilon_{cc} = \pm \frac{2l(l+1)CA^{so}}{\Delta E_{\tilde{C}-\tilde{A}}} \qquad (4.9)$$

where l is the electronic orbital angular momentum quantum number (1 for p orbitals). In formulas (4.9), the top sign again refers to the lower of the two states (i.e., to the $\widetilde{B}$ states in the ε_{bb} formula and to the $\widetilde{A}$ state in the ε_{cc} formula). In the pure precession limit, $\varepsilon_{aa} = 0$ in the $\widetilde{C}$ state, $\varepsilon_{bb} = 0$ in the $\widetilde{A}$ state and $\varepsilon_{cc} = 0$ in the $\widetilde{B}$ state. Using l =1, A^{so} = 67 cm^{-1} and the band origins for the different states, the pure precession predictions for the ε_{aa}, ε_{bb} and ε_{cc} are listed in Table 4.7.

Comparing the pure precession predictions to the observed values, the predictions for ε_{aa} are very close, however the prediction's for ε_{bb} and ε_{cc} are not as good. The pure precession model can be used as a useful tool to predict some spectroscopic constants in advance of a high resolution analysis.

Table 4.7 Pure precession prediction (cm^{-1}) for $CaNH_2$

State (To)	ε_{aa}		ε_{bb}		ε_{cc}	
	pred.	obs.	pred.	obs.	pred.	obs.
$\tilde{C}^2A_1$						
17375.167	0.0	0.9985	-0.054	-0.03966	-0.041	0.03084
$\tilde{B}^2B_1$						
15885.282	-8.31	-7.6194	0.054	-0.03673	0.0	0.07914
$\tilde{A}^2B_2$						
15464.367	8.31	8.237	0.0	0.00597	0.041	0.05526

4.4 The molecular structure of $CaNH_2$

Although three rotational constants, A, B and C are obtained from the measured spectra, it is still not possible to derive all three geometrical parameters, r_{CaN}, r_{NH} and θ_{HNH}. For a planar molecule like $CaNH_2$ $I_c = I_a + I_b$ so that only two independent geometrical parameters can be determined for each state. In order to obtain an r_0 structure the rotational constants of another isotopomer, such as $CaND_2$, has to be analyzed. For the moment since we do not have the spectra of $CaND_2$, we can only make some approximations. It is a reasonable approximation to constrain the value of r_{NH} to that of NH_2 and to assume that the molecule is planar (5). In this way the geometrical constants of the ground states can be derived. When r_{NH}=1.025 Å was used, r_{CaN}=2.122(6) Å and θ_{HNH}=106.0°.

4.5 Conclusion

In this chapter, the analysis of the 0 -1, 1 - 0 and 2 - 1 sub-bands of the $CaNH_2$ $\tilde{B}^2B_1 - \tilde{X}^2A_1$ transition and the 0 - 0 and 1 - 1 sub-bands of the $CaNH_2$ $\tilde{C}^2A_1 - \tilde{X}^2A_1$ transition are discussed. Observed line positions are fitted by a nonlinear least squares fitting procedure. Very good molecular constants are obtained.

Because the $\tilde{B}^2B_1 - \tilde{X}^2A_1$ transition is a perpendicular transition, the spectrum was well resolved, and the line positions can be easily assigned. For the $\tilde{C}^2A_1 - \tilde{X}^2A_1$

transition, however, because it is a parallel transition, the lines from different sub-bands are overlapped with each other and the analysis of the spectrum is much more difficult.

The geometrical structure of the $CaNH_2$ molecule is also determined. The small moment inertial defect ($\Delta = I_c - I_a - I_b$) shows that $CaNH_2$ is basically a planar molecule.

4.6 References

1. R. F. Wormsbecher, M. Trkula, C.M. Martner, R.E. Penn, and D.O. Harris, J. Mol. Spectrosc. 97, 29 (1983).
2. R. F. Wormsbecher, R.E. Penn, and D.O. Harris, J. Mol. Spectrosc. 97 , 65 (1983).
3. A.M. Bopegedera, C.R. Brazier, and P.F. Bernath, J. Phys. Chem. 91, 2779 (1987).
4. C.J. Whitham and Ch. Jungen, J. Chem. Phys. 93, 1001 (1990).
5. A.J. Marr, M. Tanimoto, D. Goodrige, and T.C. Steimle, J. Chem. Phys. 103, 4466 (1995).
6. C.H. Townes and A.L. Schawlow, Microwave Spectroscopy (Dover, New York, 1975).
7. C.T. Scurlock, T. Henderson, S. Bosely, K.Y. Jung, and T.C. Steimle, J. Chem. Phys. 100, 5481 (1994)
8. J.K.G. Watson, J. Chem. Phys., 46, 1935 (1967); 48, 4517 (1968)
9. E. Hirota, High-resolution Spectroscopy of Transient Molecules, Springer (1985)
10. C.N. Jarman and P.F. Bernath, J. Chem. Phys. 98, 6697 (1993)

11. Z. Morbi , C. Zhao, P. F. Bernath, J. Chem. Phys. 106, 4860 (1997)

CHAPTER 5

LASER EXCITATION SPECTROSCOPY OF $SrNH_2$

5.1 Introduction

In the previous chapter calcium monoamide was studied, in this chapter we will discuss the spectroscopic study of the strontium amide radical, $SrNH_2$. Just like in the calcium amide case, the electronic structure of $SrNH_2$ can be pictured using a one electron model. However, because strontium is heavier than calcium, the bonding may be slightly different. It is interesting to find out how $CaNH_2$ and $SrNH_2$ differ from each other.

The earliest work on the strontium amide was carried out by D. O. Harris and co-workers. They observed chemiluminescent emission from $SrNH_2$ and $CaNH_2$ (1). The $\tilde{B}^2B_1 - \tilde{X}^2A_1$ and $\tilde{A}^2B_2 - \tilde{X}^2A_1$ transitions of $SrNH_2$ were rotationally analyzed (2). The rotational constants for the $\tilde{A}^2B_2 - \tilde{X}^2A_1$ transition were successfully obtained, however, for the $\tilde{B}^2B_1 - \tilde{X}^2A_1$ transition, the spectrum was difficult to analyze because of a perturbation.

In this chapter the rotational analysis of the $\tilde{C}^2A_1 - \tilde{X}^2A_1$ transition will be discussed. The $\tilde{C}^2A_1 - \tilde{X}^2A_1$ transition is a parallel transition, and the different K sub-bands are overlapped, making the analysis difficult. In a supersonic beam, only the K′ = 0 to K″ =0 and K′ = 1 to K″ =1 sub-bands are seen.

5.2 Experimental

The experiment was also carried out with the supersonic molecular beam spectrometer. The conditions are almost the same as those described in the previous chapter except that a strontium rod was used instead of a calcium rod. The spectra were recorded by using both Ar and He as the carrier gases in order to obtain spectra at different temperatures. Kiton red dye centered at 620 nm was used for the cw 699 - 29 ring dye laser.

5.3 Results

The laser excitation spectrum of the $\tilde{C}^2A_1 - \tilde{X}^2A_1$ transition of the $SrNH_2$ is shown in Figure 5.1. The top spectrum was recorded with Ar was used as a carrier gas while the bottom spectrum was recorded with He. It is clear that even when He was used the spectrum was cooled very effectively. The rotational temperature of the Ar spectrum was about 10 K. More lines were recorded in He, but the spectrum looks much the same. The line positions are listed in Table 5.1.

The spectrum looks simple at first glance, but the assignment is not so easy because all the lines from the different K sub-bands and the different spin components overlap each other. The spectrum spreads out when the J value increases, but the lines from various branches are mingled together. This overlapping of lines is the main difference

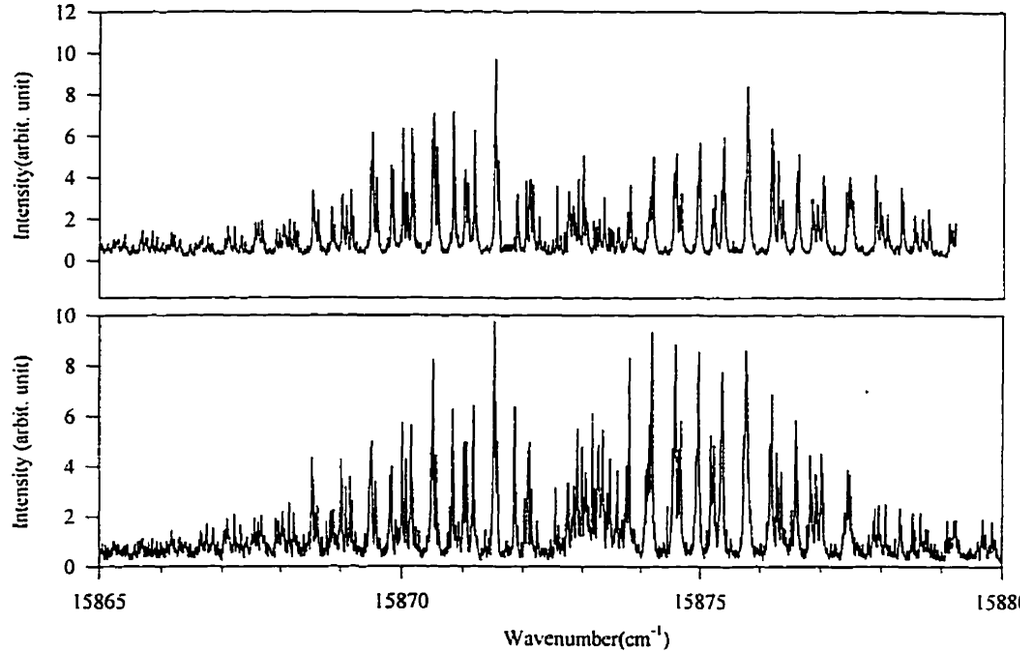

Figure 5.1 Spectrum of $\widetilde{C}^2A_1 - \widetilde{X}^2A_1$ Transition of $SrNH_2$

Table 5.1 Line positions for the $\tilde{C}^2A_1 - \tilde{X}^2A_1$ transition of $SrNH_2$

J	Observed	$\nu_{obs} - \nu_{cal}$	J	Observed	$\nu_{obs} - \nu_{cal}$
		$K_a' = 0 \leftarrow K_a'' = 0$			
	P_2			P_1	
5.5	15870.8409	0.004	3.5	15871.5364	0.002
6.5	15870.5106	0.010	4.5	15871.0394	0.000
7.5	15870.1704	0.001	5.5	15870.5657	0.017
8.5	15869.8418	-0.001	6.5	15870.0687	0.006
9.5	15869.5183	-0.003	7.5	15869.5783	-0.001
10.5	15869.1981	-0.006	8.5	15869.0930	-0.007
11.5	15868.8845	-0.006	9.5	15868.6177	-0.005
12.5	15868.5677	-0.013	10.5	15868.1407	-0.004
13.5	15868.2708	-0.002	11.5	15867.6737	0.002
14.5	15867.9739	0.006	12.5	15867.1964	0.001
15.5	15867.6720	0.009			
				R_1	
	R_2		3.5	15874.5485	-0.002
1.5	15874.6368	0.002	4.5	15874.9504	-0.005
2.5	15875.1889	0.012	5.5	15875.3657	-0.001
3.5	15875.7226	-0.002	6.5	15875.7710	-0.011
4.5	15876.2863	0.004	7.5	15876.2029	0.000
5.5	15876.8484	0.002	8.5	15876.6232	-0.002
6.5	15877.4004	-0.016	9.5	15877.0502	-0.002
7.5	15878.0042	0.008	10.5	15877.4755	-0.006
8.5	15878.5779	-0.003	11.5	15877.9091	-0.003
			12.5	15878.3477	0.002
			13.5	15878.7930	0.014

Table 5.1 (continued)

J	Observed	$\nu_{obs} - \nu_{cal}$	J	Observed	$\nu_{obs} - \nu_{cal}$
		$K_a' = 1 \leftarrow K_a'' = 1$			
	P_{11}^{1}			R_{22}^{1}	
2.5	15872.4823	0.015	1.5	15875.3307	-0.002
3.5	15872.0363	0.048	2.5	15875.8410	-0.019
4.5	15871.5092	0.015	3.5	15876.3931	-0.005
5.5	15871.0001	0.004	4.5	15876.9385	-0.006
6.5	15870.5064	0.008	5.5	15877.5005	0.001
7.5	15870.0087	0.007	6.5	15878.0843	0.026
8.5	15869.5050	-0.003	7.5	15878.6496	0.025
9.5	15869.0263	0.005			
10.5	15868.5344	-0.002		P_{11}^{0}	
11.5	15868.0657	0.005	4.5	15871.0698	-0.004
12.5	15867.5920	0.003	5.5	15870.5233	-0.018
			6.5	15870.0196	-0.000
	R_{11}^{1}		7.5	15869.5049	-0.005
1.5	15874.1949	-0.016	8.5	15869.0096	-0.000
2.5	15874.5968	-0.009	9.5	15868.5159	-0.002
3.5	15874.9838	-0.014	10.5	15868.0389	0.005
4.5	15875.3824	-0.009	11.5	15867.5569	0.003
5.5	15875.7893	0.000	12.5	15867.0833	0.007
6.5	15876.2046	0.013			
7.5	15876.5966	-0.003		R_{11}^{0}	
8.5	15877.0185	0.001	2.5	15874.1966	-0.015
9.5	15877.4455	0.003	3.5	15874.5785	0.000
10.5	15877.8808	0.003	4.5	15874.9588	0.003
11.5	15878.3194	-0.002	5.5	15875.3490	0.002
12.5	15878.7647	-0.013	6.5	15875.7576	0.008
			7.5	15876.1729	0.010
	P_{22}^{1}		8.5	15876.5916	0.006
4.5	15871.8601	-0.003	9.5	15877.0235	0.008
5.5	15871.5092	-0.000	10.5	15877.4521	0.001
6.5	15871.1611	-0.001	11.5	15877.8824	-0.007
7.5	15870.8292	0.008	12.5	15878.3194	-0.010
8.5	15870.4900	0.006	13.5	15878.7647	-0.005
9.5	15870.1454	-0.003			
10.5	15869.8152	-0.003			
11.5	15869.4883	-0.003			
12.5	15869.1614	-0.007			
13.5	15868.8428	-0.006			
14.5	15868.5293	-0.005			
15.5	15868.2207	-0.002			
16.5	15867.9172	-0.000			
17.5	15867.6220	0.005			

Table 5.2 Fitted spectroscopic constants for the low-lying electronic states of $SrNH_2$ (cm^{-1})

	$\tilde{X}^2A_1$ [a]	$\tilde{A}^2B_1$ [a]	$\tilde{C}^2A_1$
T_{00}	--	14230.6237(34)	15872.986(01)
A	13.142570(78)	12.10285(12)	13.603(84)
B	0.2265478(17)	0.2307143(52)	0.2354(85)
C	0.2220268(17)	0.2260600(56)	0.2152(65)
ε_{aa}	0.00293(37)	30.01872(22)	1.675(51)
ε_{bb}	0.001805(25)	0.037435(85)	-0.296(12)
ε_{cc}	0.002882(28)	0.272902(52)	0.019(38)
Δ_K	0.0022682(74)	0.003455(18)	0.002(82)
Δ_{NK}	0.000045309(77)	0.00003279(12)	-0.0036(98)
Δ_N	$1.934(26)\times10^{-7}$	$1.878(27)\times10^{-7}$	

[a] Fixed to the values of reference(2).

between parallel and perpendicular transitions. A relatively weak Q branch was recorded at around 15873 cm^{-1}. The line positions were fitted using the model described in the previous chapter with the ground state constants fixed to that of reference (2), and the molecular constants are listed in Table 5.2.

5.4 Discussion

The analysis procedure was given in the previous chapter, so that only the difference between the parallel and perpendicular transitions will be discussed here.

The molecular constants of the $\tilde{A}^2B_2 - \tilde{X}^2A_1$ transition derived by Brazier and those of the $\tilde{C}^2A_1 - \tilde{X}^2A_1$ transition obtained in our work are listed in Table 5.2. The molecular constants predicted by the pure precessing model for all three transitions are listed in Table 5.3.

From Table 4.5, the diagonal matrix element of the spin-rotation part of the Hamiltonian is:

$$\langle NKSJ|H_{sr}|NKSJ\rangle = -[\Gamma(NSJ)/2N(N+1)]\{\varepsilon_{aa}K^2 + (\varepsilon_{bb}+\varepsilon_{cc}) \times[N(N+1)-K^2]/2\} \qquad 5.1$$

The K dependent term is proportional to ε_{aa} and from Table 5.3, the ε_{aa} value of the $\tilde{C}^2A_1$ state is predicted to be 0 by the pure precession model. The values of ε_{bb} and ε_{cc} are also relatively small so that the spin-rotation part of the Hamiltonian is much smaller in

the $\tilde{C}^2A_1$ state than in the $\tilde{A}^2B_2$ and $\tilde{B}^2B_1$ states. In the $\tilde{A}^2B_2$ and $\tilde{B}^2B_1$ states a big ε_{aa} value and the selection rule $\Delta K = \pm 1$ causes the spectrum for different K sub-bands to be shifted away from each other. Thus we see a very well resolved spectrum for the $\tilde{A}^2B_2 - \tilde{X}^2A_1$ and $\tilde{B}^2B_1 - \tilde{X}^2A_1$ transitions and a very dense spectrum for $\tilde{C}^2A_1 - \tilde{X}^2A_1$ transition even under molecular beam conditions.

Table 5.3 Pure precession predictions in (cm^{-1}) for $SrNH_2$

State (T_o)	ε_{aa}		ε_{bb}		ε_{cc}	
	pred.	obs.	pred.	obs.	pred.	obs
$\tilde{C}^2A_1$						
15872.986	0.0	1.675	-0.207	-0.296	-0.146	0.019
$\tilde{B}^2B_1$						
14689.836	-28.9	-34.131	0.207	0.1536	0.0	0.1583
$\tilde{A}^2B_2$						
14230.6237	28.9	30.01872	0.0	0.001805	0.146	0.002882

5.5 Molecular structure

As in the $CaNH_2$ case, the ground state molecular structure of $SrNH_2$ can be estimated by fixing the NH bond length to the value found in NH_2. Using r_{NH}=1.025 Å as derived for NH_2, gives r_{SrN}= 2.2511Å and θ_{HNH}=102.19°. The inertial defect, Δ, is 0.23 amu Å^2. For comparision, the molecular geometries of $CaNH_2$ and $SrNH_2$ are listed in Table 5.4. The Sr-N bond length is greater than the Ca-N bond length because the Sr atom has a larger diameter than Ca. The ground state moment of inertial defect for $SrNH_2$ is bigger than that for $CaNH_2$. Table 5.4 also lists parameters for the excited states of $CaNH_2$. The values for the $\tilde{A}$ and $\tilde{B}$ states are calculated by using the average value of the A rotational constants derived from the analysis. We can see that the Ca-N bond length and H-N-H bond angles are very similar for the different states but the moment of inertia defects shows considerable variation. For the $\tilde{B}$ state, a large Δ value of 0.618 is obtained because of the interactions between $\tilde{A}$, $\tilde{B}$ and $\tilde{C}$ states. Averaging the A constants for $\tilde{A}$ and $\tilde{B}$ states has only partly corrected for these interactions. For $SrNH_2$, the constants for the $\tilde{C}$ state differ considerably from those of the ground state, suggesting that these may be a problem with the fits.

Table 5.4 Molecular structure of $SrNH_2$

Molecule	State	r_{NH} [a] /Å	r_{SrN} or r_{CaN} /Å	θ_{HNH}	Δ/amu Å^2
$CaNH_2$	$\tilde{A}$	1.025	2.0957	103.34°	0.136
	$\tilde{B}$	1.025	2.1165	103.34°	0.618
	$\tilde{C}$	1.025	2.1027	103.24°	0.012
	$\tilde{X}$	1.025	2.1189	102.65°	0.167
$SrNH_2$	$\tilde{A}$	1.025	2.4318	101.41°	0.235
	$\tilde{B}$	1.025	2.4661	101.41°	1.146
	$\tilde{C}$	1.025	2.4045	99.80°	5.483
	$\tilde{X}$	1.025	2.2511	102.19°	0.232

[a] fixed.

5.6 Conclusion

In this chapter the work on the $\tilde{C}^2A_1 - \tilde{X}^2A_1$ transition of $SrNH_2$ is described. Because of the cooling effect in the supersonic beam, only the 0 - 0 and 1 - 1 K sub-bands were recorded which makes it possible to analyze a very dense spectrum. From the geometrical structure we see that $SrNH_2$ has a slightly bigger moment of inertial defect than $CaNH_2$ but since the defects are relatively small, we can say that both are planar molecules in their ground states.

5.7 References

1. R. F. Wormsbecher, M. Trkula, C. Martner, R. E. Penn and D. O. Harris, J. Mol. Spectrosc., 97, 29 (1983).

2. C. R. Brazier, P. F. Bernath, unpublished.

CHAPTER 6

HIGH RESOLUTION LASER EXCITATION SPECTROSCOPY OF CALCIUM MONOMETHOXIDE $CaOCH_3$

6.1 Introduction

The interaction of metals with organic molecules is very important in the development of modern chemistry. A large number of alkaline earth metal-containing free radicals have been studied using the technique of laser excitation spectroscopy. These molecules were made by reaction of alkaline earth atoms (Ca, Sr, Ba) with alcohols (1, 2), carboxylic acids (1), isocyanic acid (3), cyclopentadiene (4), metal alkyls (5), amines (6), and acetylene (6, 7). The free radical product molecules were formed by combining one alkaline earth metal atom and one ligand group.

Laser excitation spectroscopy of the alkaline earth monomethoxides was first carried out for $SrOCH_3$ (8), using methyl nitrite (CH_3ONO) to react with gas-phase strontium atoms. Only low resolution spectra were recorded and a vibrational analysis of the $\tilde{A}^2E-\tilde{X}^2A_1$ and $\tilde{B}^2A_1-\tilde{X}^2A_1$ transitions were reported. Later, a high resolution spectrum of the 0 - 0 band of the $\tilde{A}^2E-\tilde{X}^2A_1$ transition of $SrOCH_3$ was recorded by combining laser excitation spectroscopy and narrow band fluorescence detection in a Broida oven (9). In this experiment methanol was used instead of methyl nitrite in the

reaction and a second laser was used to excite the strontium atom to the first excited $^3P_1$ state.

In this chapter, a preliminary high resolution analysis of the $\tilde{A}^2E - \tilde{X}^2A_1$ transition of $CaOCH_3$ will be reported. Because $CaOCH_3$ should have the same structure as $SrOCH_3$, the Ca-O-C bond angle should be 180° (9), which will give a prolate symmetric top molecule with C_{3v} symmetry. The off-axis hydrogens in $CaOCH_3$ do not perturb the spin-orbit coupling in the $\tilde{A}^2E$ state, so that a spin-orbit splitting similar to the value of 65 cm^{-1} for the corresponding $\tilde{A}^2\Pi$ state of CaOH is expected.

6.2 Experimental

The $CaOCH_3$ experiment was also carried out in the supersonic molecular beam spectrometer described in previous chapters. Ca metal was vaporized by the 532 nm radiation from the Nd/YAG laser. About 60 psi of Ar or He was used as carrier gas to bubble through liquid methanol. After the pulsed valve was opened the methanol mixed with the Ca plasma during the supersonic expansion into the vacuum.

Because of the spin-orbit splitting in the excited state, two spin components should appear, i.e. $^2E_{1/2}$ and $^2E_{3/2}$, in the $\tilde{A}^2E$ state. From the low resolution spectrum recorded by Brazier and coworkers, the transition to the $\tilde{A}^2E_{1/2}$ component should be at around 15917 cm^{-1} and $\tilde{A}^2E_{3/2}$ at 15982 cm^{-1}(2). From our experiment, two very strong

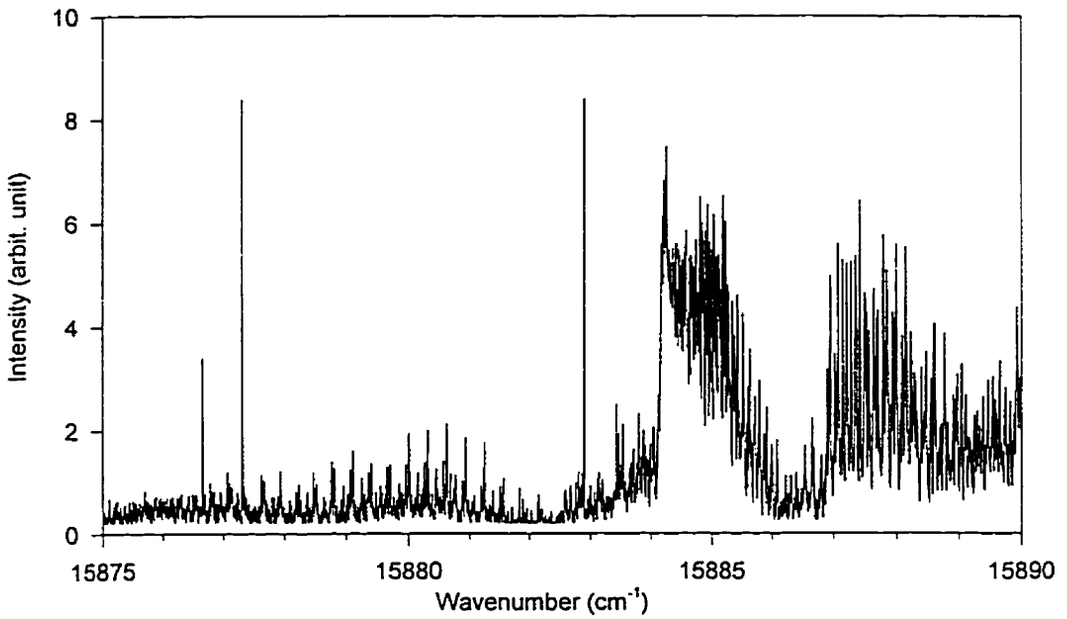

Figure 6.1 Spectrum of $\widetilde{A}^2E_{1/2} - \widetilde{X}^2A_1$ Transition of $CaOCH_3$ in He

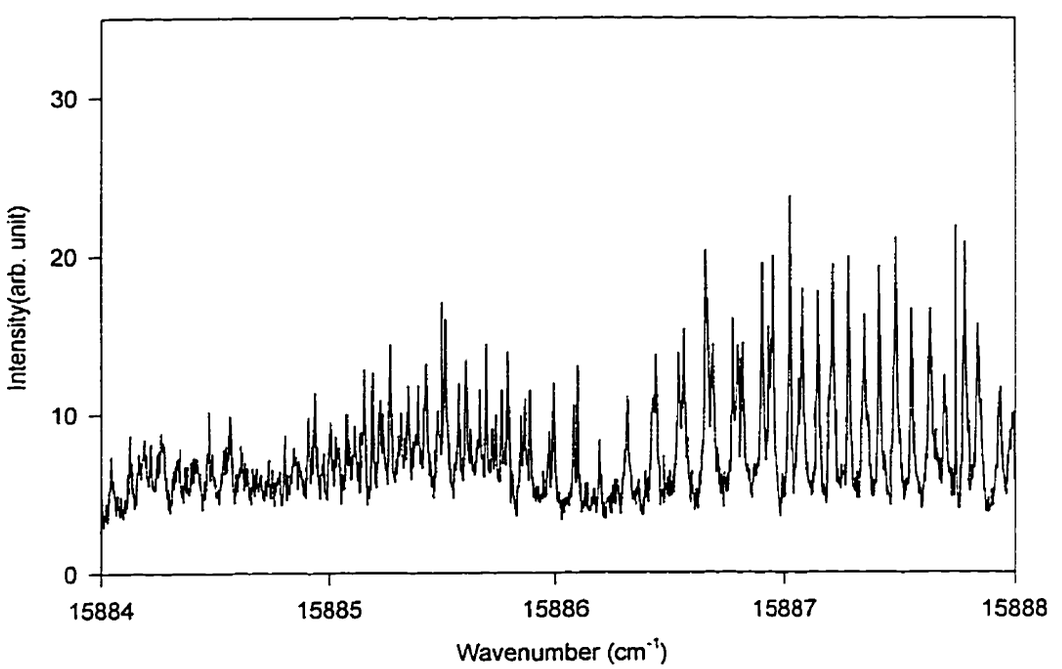

Figure 6.2 Spectrum of $\widetilde{A}^2E_{1/2} - \widetilde{X}^2A_1$ Transition of $CaOCH_3$ in Ar

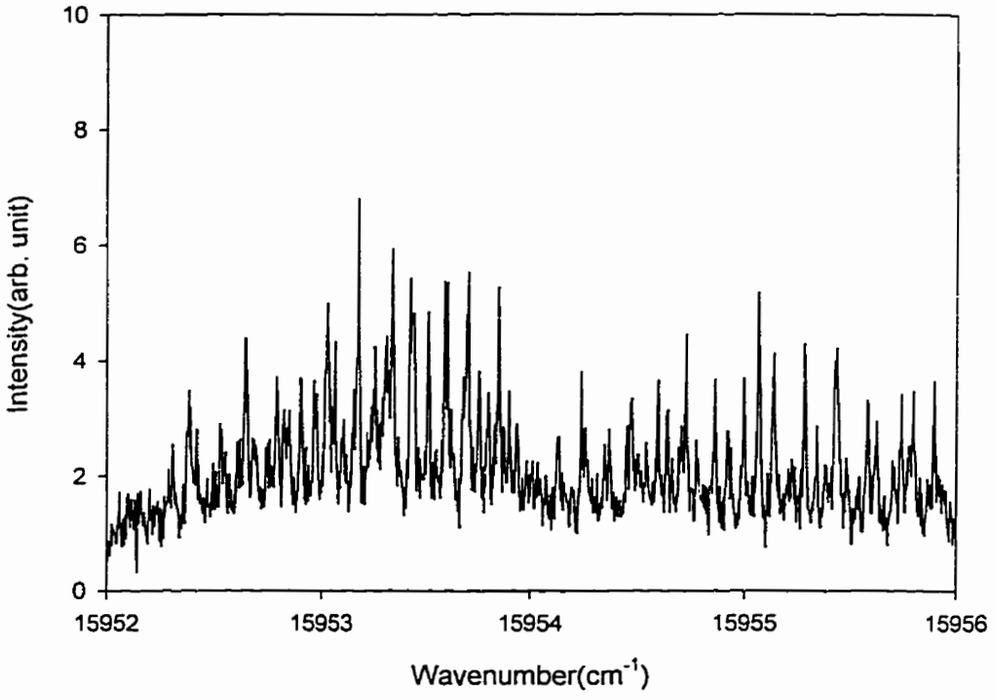

Figure 6.3 Spectrum of $\widetilde{A}^2E_{3/2} - \widetilde{X}^2A_1$ Transition of $CaOCH_3$ in Ar

features around 15886 and 15954 cm^{-1} were recorded and assigned as transitions to the $\tilde{A}^2E_{1/2}$ and $\tilde{A}^2E_{3/2}$ spin components, respectively.

6.3 Results

The branch pattern for a Hund's case (a) ^2E - $^2A_1$ transition is similar to that for a case (a) $^2\Pi$ - $^2\Sigma^+$ transition but complicated by the presence of multiple sub-bands due to K rotational structure. Each spin-orbit component of the ^2E state has six branches, 2P, 2Q and 2R which have line spacings of approximately -3B, -B(2 branches), +B(2 branches), and + 3B at low J. The selection rules are $\Delta K = \pm 1$, $\Delta J = 0, \pm 1$. In our case only the 0 -1, 1 - 0, and 2 - 1 K sub-bands were recorded because of the cooling in the supersonic beam.

The high resolution spectrum of the $^2E_{1/2}$ - $^2A_1$ transition of $CaOCH_3$ recorded in He is shown in Figure 6.1. The spectrum is not well resolved in the P branch -B region (15885 cm^{-1}) because in He the rotational temperature is above 200 K, so that the different K sub-bands are overlapped. Thus a band head forms at 15884 cm^{-1}. Another complication is that the sub-band origins are almost the same for the different K sub-bands(10). In the -3B region, the spectrum is well resolved, and is easily assigned. When the same spectrum was recorded in Ar, Figure 6.2, the lines are resolved even in the -B region because the rotational temperature is about 10 K. However, the -3B lines are missing from the cold Ar spectrum, so both spectra were used in the analysis.

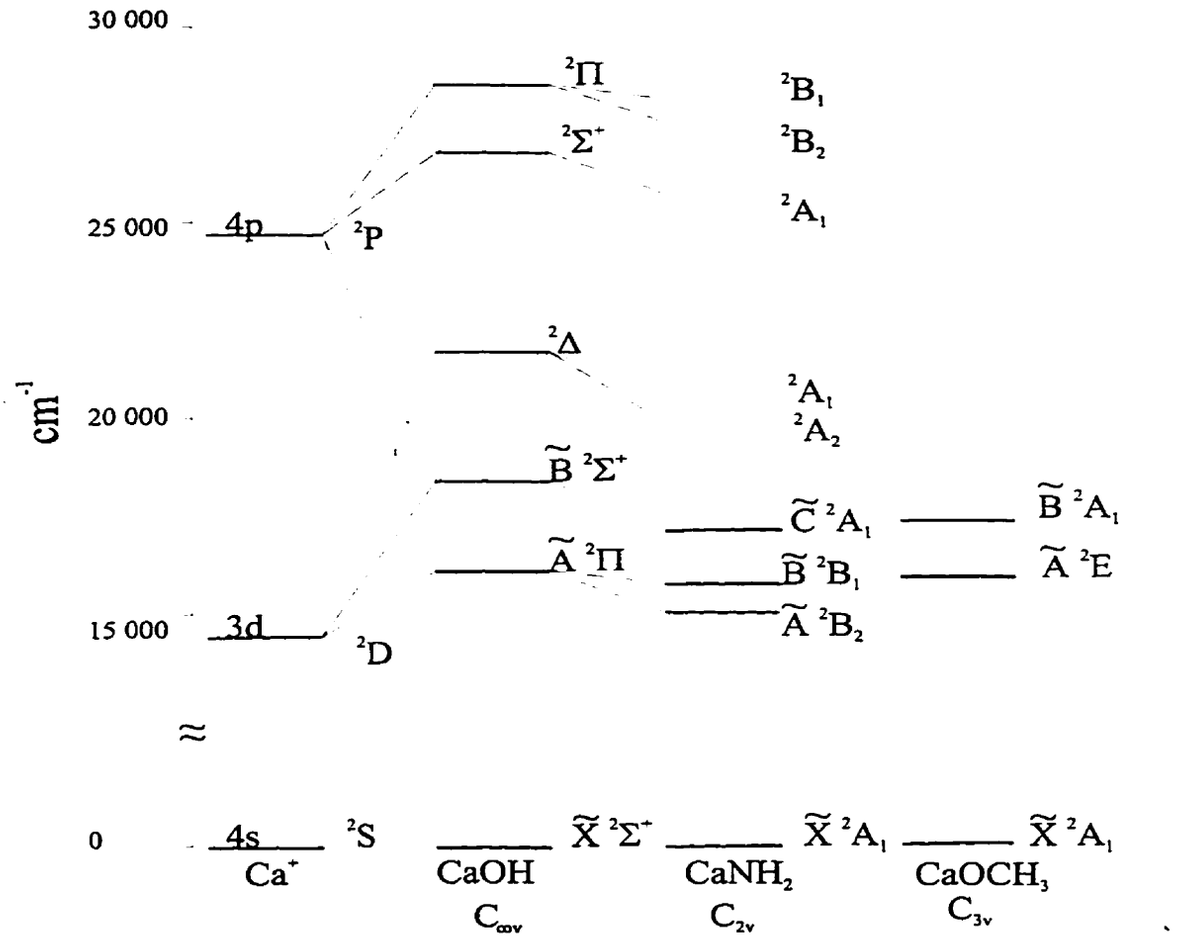

Figure 6.4 Correlation Diagram

The spectrum of $^2E_{3/2}$ - $^2A_1$ transition of $CaOCH_3$ was also recorded, Figure 6.3. Due to the complexity of this spectrum, it was not possible to make any assignments.

6.1 Discussion

A. Electronic Structure

The $\widetilde{A}^2E-\widetilde{X}^2A_1$ transition is analogous to the $\widetilde{A}^2\Pi-\widetilde{X}^2\Sigma^+$ transition of the linear CaOH and the correlation diagram is pictured in Figure 6.4. Ca has two valence electrons and when Ca and OCH_3 are combined to form a bond, one of the Ca valence electrons is given to O and this results in a very ionic bond between Ca^+ and $^-OCH_3$. There is one nonbonding valence electron centered on Ca^+. When this electron is in the 4s (a_1) orbital, one obtains the ground electronic state, $\widetilde{X}^2A_1$, while if this electron is promoted to the excited orbitals(e, a_1 etc.) one obtains the low-lying electronic states, $\widetilde{A}^2E$, $\widetilde{B}^2A_1$ and $\widetilde{C}^2E$ etc..

In the ^2E state, the total electron spin angular momentum S, the orbital angular momentum L, the rotational angular momentum R, and the total angular momentum J can be considered to be quantized along the top a-axis in the molecule-fixed axis system. For the $\widetilde{A}$ state this is analogous to the Hund's case (a) limit for diatomic molecules. The separation of 65 cm^{-1} between the $^2E_{1/2}$ and the $^2E_{3/2}$ spin components is about the same as the spin-orbit splitting of the CaOH, consistent with a ^2E state that is belongs to Hund's

case (a). Figure 6.5 shows Hund's case (a) coupling for the ^{2}E state where the projections of N, S and J along the prolate top axis are represented as K, Σ, and P, respectively, with P = K + Σ. The projection of L on the top axis is ζ_ed, where d is a Jahn-Teller quenching parameter.

When the Jahn-Teller effect is weak, ζ_ed correlates to Λ of the linear CaOH molecule with Λ = ±1 for the corresponding $\tilde{A}\,^2\Pi$ electronic state. In this case, d ~ ±1 and ζ_e is also close to 1, and the spin-orbit energy formulas are

$$E_{SO} = A\Lambda\Sigma, \text{ where } A = 65 \text{ cm}^{-1} \text{ for CaOH}$$

and

$$E_{SO} = a\,\zeta_e d\Sigma, \quad \text{where} \quad a\,\zeta_e d = 67 \text{ cm}^{-1} \text{ for } CaOCH_3$$

The Jahn-Teller effect for the ^{2}E state of $CaOCH_3$ is small.

B. Rotational structure

$CaOCH_3$ is a prolate symmetric top molecule and the N^2 form of the rotational Hamiltonian will be used (18, 19, 23),

$$\hat{H} = \hat{H}_{ROT} + \hat{H}_{CD} + \hat{H}_{COR} + \hat{H}_{SO}$$

for the ^{2}E state and

$$\hat{H} = \hat{H}_{ROT} + \hat{H}_{CD} + \hat{H}_{SR}$$

for the $^2A_1$ state, where

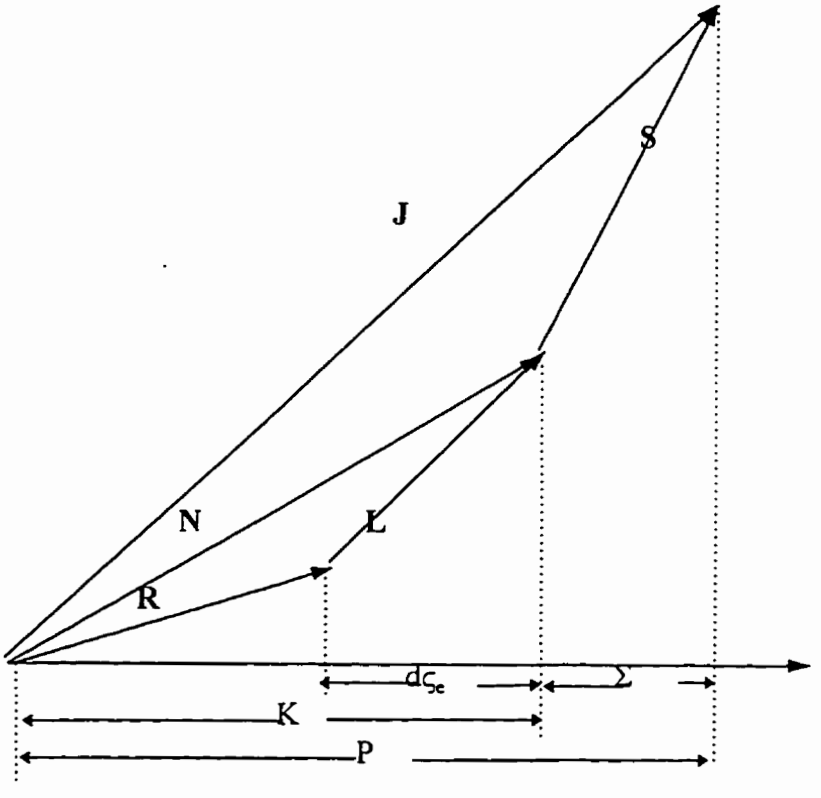

Figure 6.5 Hund's Case (a) Coupling for a ^2E State

$$\hat{H}_{ROT} = (A - B)\,\hat{N}_z^2 + B\hat{N}^2$$

is the rotational part,

$$\hat{H}_{CD} = -D_N\hat{N}^4 - D_{NK}\hat{N}^2\hat{N}_z^2 - D_K\hat{N}_z^4$$

is the centrifugal distortion part,

$$\hat{H}_{COR} = -2A\hat{N}_z\hat{L}_z + \eta_e\hat{N}^2\hat{N}_z\hat{L}_z + \eta_K\hat{N}_z^3\,\hat{L}_z$$

is the first-order electronic Coriolis interaction term,

$$\hat{H}_{SO} = a\hat{L}_z\hat{S}_z$$

is the spin-orbit interaction term,

$$\hat{H}_{SR} = \varepsilon_{aa}\hat{N}_z\hat{S}_z + \tfrac{1}{4}(\varepsilon_{bb} + \varepsilon_{cc})(\hat{N}_+\hat{S}_- + \hat{N}_-\hat{S}_+)$$

is the spin-rotation interaction term with

$$\hat{N} = \hat{J} - \hat{S}$$

defined as the total angular momentum without spin and

$$\hat{N}_z = \hat{J}_z - \hat{S}_z$$

is the projection of the total angular momentum along the top axis.

The Hund's case (a) ^2E - $^2A_1$ transition should have a similar branch pattern as a $^2\Pi$ - $^2\Sigma$ transition but complicated by the presence of multiple sub-bands due to the K rotational structure. There are six branches spaced by approximately - 3B, - B (2), + B (2), and + 3B at low J. The -B and + B branches are doubled due to the spin-rotation interaction in the ground state but we were not able to resolve this splitting because only low J lines were recorded.

Figure 6.6 is the energy level diagram for the K′ = 1 to K″ = 0 sub-band transition. P_1 and Q_{12} are the -B branches and they are not resolved. Q_1 is the +B branch, P_{12} the -3B branch and R_1 the +3B branch. The first line in -B branch is $Q_{12}(0.5)$ and the first line in +B branch is $Q_1(0.5)$ and there is about a 2B interval between them. For the -3B and +3B branches the first lines are $P_{12}(1.5)$ and $R_1(0.5)$, respectively, and there is band gap of about 9B at the origin.

Figure 6.7 is the energy level diagram for the K′ = 0 to K″ = 1 sub-band transition. The energy levels for this transition are very similar to that of the K′ = 1 to K″ = 0 sub-band transition except that the $Q_1(0.5)$ line is missing from the spectrum because the ground state N starts at 1. The band gap spacing between the two first lines is about 3B.

Figure 6.8 is the energy level diagram for the K′ = 2 to K″ = 1 sub-band transition. In this transition two lines ($Q_{12}(0.5)$ and $Q_1(0.5)$) are missing from the spectrum and this make the band gap between two first lines about 4B.

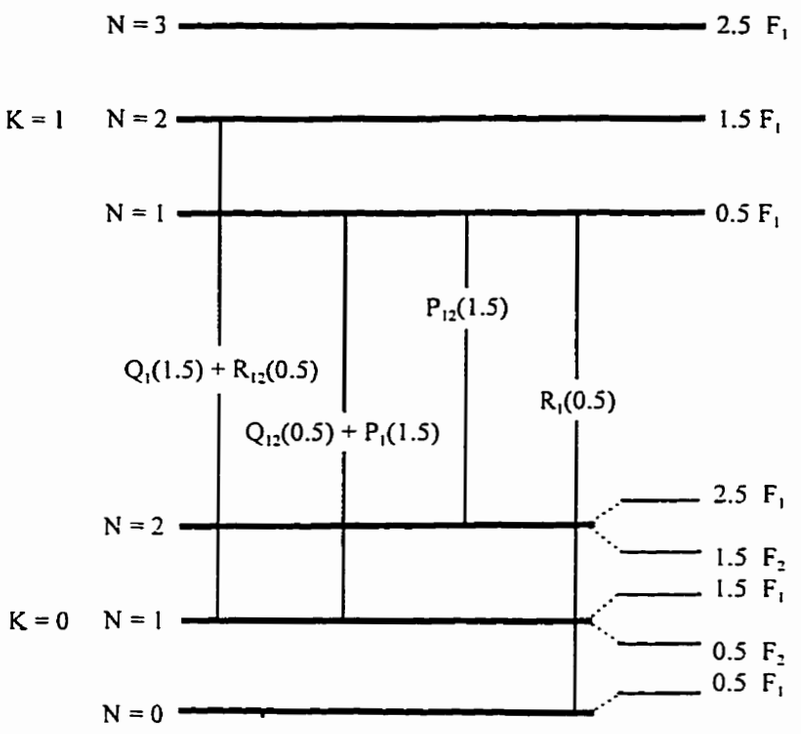

Figure 6..6 Energy diagram for the K′ = 1 - K″ = 0 (K_R= 0 - 0) sub-band of $^2E_{1/2}$ - $^2A_1$ transition, where Q_{12} and P_1 are the -B branches, Q_1 and R_{12} are the +B branches, P_{12} is the -3B branch and R_1 is the +3B branch.

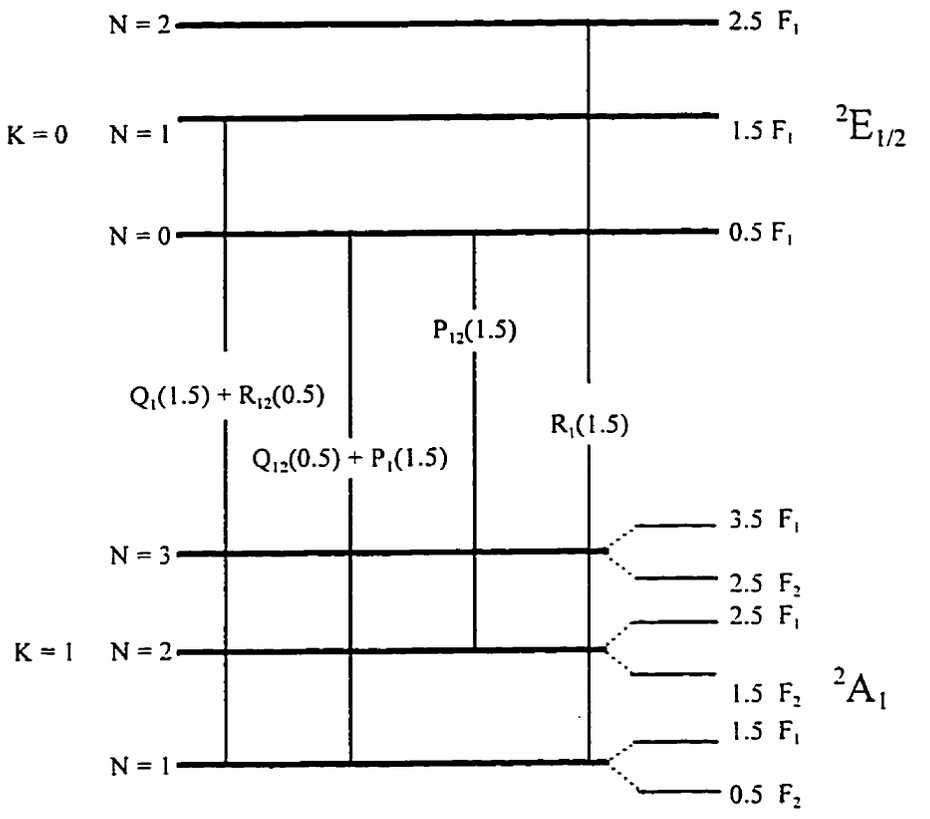

Figure 6.7 Energy diagram for the K′ = 0 - K″ = 1 (K_R= 1 - 1) sub-band of $^2E_{1/2}$ - $^2A_1$ transition, where Q_{12} and P_1 are the -B branches, Q_1 and R_{12} are the +B branches, P_{12} is the -3B branch and R_1 is the +3B branch.

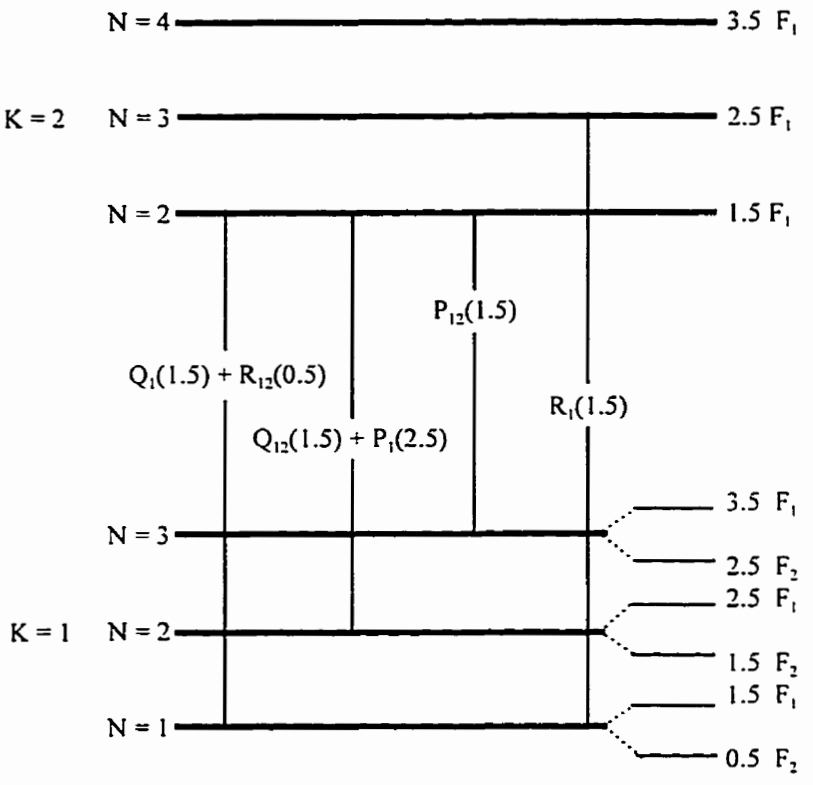

Figure 6.8 Energy diagram for the K′ = 2 - K″ = 1 (K_R= 1 - 1) sub-band of $^2E_{1/2}$ - $^2A_1$ transition, where Q_{12} and P_1 are the -B branches, Q_1 and R_{12} are the +B branches, P_{12} is the -3B branch and R_1 is the +3B branch.

The spectrum of the $^2E_{1/2}$ - $^2A_1$ transition in Ar is shown in Figure 6.2, only the low J lines of the +B and -B branches are seen in this region and the +3B and -3B branches are weak. Figure 6.1 Shows the spectrum recorded in He for the same transition. The spectrum close to the band origin is very dense and there is a very strong band head caused by the overlapping of the different sub-bands. To the lower wavenumber side of the band head are some well resolved lines, assigned to the -3B branches. The observed transition wavenumbers used in the fit are listed in Table 6.1 and the molecular constants determined from the fit are given in Table 6.2.

6.5 Conclusion

The $^2E_{1/2}$ - $^2A_1$ transition of $CaOCH_3$ was rotationally analyzed for the first time. The high resolution spectrum was recorded using the supersonic beam spectrometer. Preliminary molecular constants were obtained with a nonlinear least squares fitting program. The Jahn-Teller effect was found to be small in the $\tilde{A}^2E$ state.

Table 6.1 Observed lines for the $\tilde{A}^2E - \tilde{X}^2A_1$ transition of $CaOCH_3$ (cm^{-1})

	K′ = 1, K″ = 0	
J	$Q_{12} + P_1$	
0.5	15886.08992	-0.02089
1.5	15885.98652	-0.00962
2.5	15885.88478	0.00175
3.5	15885.78721	0.01568
4.5	15885.69215	0.03044
5.5	15885.59875	0.04509
6.5	15885.52035	0.06287
7.5	15885.42863	0.08531
	$Q_1 + R_{12}$	
0.5	15886.30704	-0.03768
1.5	15886.43182	-0.03214
2.5	15886.55441	-0.03034
3.5	15886.68033	-0.02683
4.5	15886.80625	-0.02499
5.5	15886.93968	-0.01741
6.5	15887.0731	-0.01172
7.5	15887.21472	0.00015
8.5	15887.34913	0.00266
9.5	15887.48892	0.00821
10.5	15887.63266	0.01519
11.5	15887.78193	0.02496
	P_{12}	
12.5	15881.88517	-0.01424
13.5	15881.56495	-0.00832
14.5	15881.24806	-0.00229
15.5	15880.92784	-0.00308
16.5	15880.61596	0.00069
17.5	15880.30908	0.00536
18.5	15880.00387	0.00727
19.5	15879.70032	0.00606
20.5	15879.39511	-0.00196
21.5	15879.09657	-0.00886
22.5	15878.80637	-0.01338
	K′ = 0, K″ = 1	
	$Q_1 + R_{12}$	
1.5	15886.4176	-0.01236
2.5	15886.5316	-0.01865
3.5	15886.6499	-0.02223
4.5	15886.7703	-0.02531
5.5	15886.9072	-0.02356
6.5	15887.0208	-0.02689
7.5	15887.1478	-0.02872
8.5	15887.2821	-0.0253
9.5	15887.4175	-0.02299
10.5	15887.5541	-0.02189
11.5	15887.6971	-0.01701
	$Q_{12} + P_1$	
0.5	15886.0747	-0.00036
1.5	15885.9704	0.00954
2.5	15885.8605	0.01733
3.5	15885.7629	0.02704
4.5	15885.6671	0.04154
5.5	15885.5736	0.0567
6.5	15885.4709	0.06902
7.5	15885.3898	0.08485
	P_{12}	
13.5	15881.51158	-0.01714
14.5	15881.19469	-0.00952
15.5	15880.8778	-0.00526
16.5	15880.56592	0.00035
17.5	15880.25904	0.00697
18.5	15879.95383	0.01096
19.5	15879.65196	0.01363
20.5	15879.35342	0.01459
21.5	15879.05488	0.01013
22.5	15878.76301	0.0065
23.5	15878.46947	-0.00507
24.5	15878.18094	-0.01837

Table 6.1 (continued)

	K′ = 2, K″ = 1	
	Q1 + R12	
1.5	15886.4184	-0.01437
2.5	15886.5359	-0.0157
3.5	15886.6606	-0.01083
4.5	15886.7917	-0.00057
5.5	15886.9251	0.01089
6.5	15887.0627	0.02537
7.5	15887.1993	0.03753
8.5	15887.3391	0.05143
9.5	15887.4645	0.0493
	$Q_{12} + P_1$	
1.5	15885.9456	-0.01807
2.5	15885.8467	-0.00232
3.5	15885.7381	0.00294
4.5	15885.6274	0.00517
	P_{12}	
15.5	15880.76439	-0.05678
16.5	15880.44917	-0.04544
17.5	15880.14897	-0.02247
18.5	15879.84375	-0.00825
19.5	15879.54355	0.00692
20.5	15879.24668	0.02098
21.5	15878.95314	0.03352

Table 6.2 Molecular constants for the 0 - 0 Band of $\tilde{A}^2E - \tilde{X}^2A_1$ Transition of $CaOCH_3$ (cm^{-1})

constants	$\tilde{X}^2A_1$	
A		5.18511[a]
B		0.1173(49)
DK		0.02(90)
ε_{aa}		-0.00178[a]
$\varepsilon_{bb} + \varepsilon_{cc}$		0.001586[a]
	$\tilde{A}^2E$	
T		15924.66(20)
a_{so}		66.8[b]
$A\xi_{st}$		5.088(63)
A		5.153386(93)
B		0.11823(92)
D_K		0.003(63)
D_{NK}		0.20655(23)
D_N		$-8.4(44)\times10^{-7}$

[a] Fixed to the value in Reference 9

[b] Fixed to the value of CaOH

6.6 References

1. C. R. Brazier, P. F. Bernath, S. Kinsey-Nielson, and L. C. Ellingboe, J. Chem. Phys. 82, 1043 (1985).

2. C. R. Brazier, L. C. Ellingboe, S. Kinsey-Nielson, and P. F. Bernath, J. Am. Chem. Soc. 108, 2126 (1986).

3. L. C. Ellingboe, A. M. R. P. Bopegedera, C. R. Brazier, and P. F. Bernath, Chem. Phys. Lett. 126, 285 (1986).

4. L. C. Ellingboe and P. F. Bernath, J. Am. Chem. Soc. 108, 5017 (1986).

5. C. R. Brazier, P. F. Bernath, J. Chem. Phys. 86, 5918 (1987).

6. A. M. R. P. Bopegedera, C. R. Brazier, P. F. Bernath, J. Phys. Chem. 91, 2779 (1987).

7. A. M. R. P. Bopegedera, C. R. Brazier, P. F. Bernath, Chem. Phys. Lett. 136, 97 (1987).

8. R. F. Wormsbecher and R. D. Suenram, J. Mol. Spectrosc. 95, 391 (1982).

9. L. C. O'Brien, C. R. Brazier, P. F. Bernath, J. Mol. Spectrosc. 130, 33 (1988).

10. C. R. Brazier and P. F. Bernath, J. Chem. Phys. 91, 4548 (1989).